Tectono-stratigraphic evolution of the intermontane Tarom Basin (NW sectors of the Arabia-Eurasia collision zone): insights into the vertical growth of the Iranian Plateau margin

M. Paknia[1], P. Ballato[1], M. Mattei[1], G. Heidarzadeh[2], F. Cifelli[1], J. Hassanzadeh[3], G. Vezzoli[4], M. Mirzaie Ataabadi[5] and M.R. Ghassemi[6]

[1]Department of Science, University of Roma Tre, Rome, Italy

[2]Institute of Earth and Environmental Sciences, University of Potsdam, Potsdam, Germany

[3]Division of Geological & Planetary Sciences, California Institute of Technology Pasadena, Pasadena, CA, USA

[4]Department of Earth and Environmental Sciences, University of Milano-Bicocca, Milan, Italy

[5]Department of Geology, Faculty of Science, University of Zanjan, Zanjan, Iran

[6]Research Institute for Earth Sciences, Geological Survey of Iran, Tehran, Iran

Corresponding author: Mohammad Paknia (Mohammad.Paknia@uniroma3.it)

Key Points:

- In the Tarom Basin arc volcanism terminated at ~38-36 Ma, while intermontane synorogenic deposition occurred from ~16.5 to < 7.6 Ma
- The Iranian Plateau formed in the broken retroforeland of the Arabia-Eurasia collision zone
- Crustal shortening and thickening cannot be responsible for the vertical growth of the

Iranian Plateau margin

Abstract

The intermontane Tarom Basin of NW Iran (Arabia-Eurasia collision zone) is located at the transition between the Iranian Plateau (IP) to the SW and the Alborz Mountains to the NE. This basin was filled by Late Cenozoic synorogenic red beds that retain first-order information on the erosional history of adjacent topography, the vertical growth of the plateau margin and its lateral (orogen perpendicular) expansion. Here, we perform a multidisciplinary study including magnetostratigraphy, sedimentology, geochronology and sandstone petrography on these red beds. Our data show that widespread Eocene arc volcanism in NW Iran terminated at ~ 38-36 Ma, while intrabasinal synorogenic sedimentation occurred between ~ 16.5 and < 7.6 Ma, implying that the red beds are stratigraphically equivalent to the Upper Red Formation. After 7.6 Ma, the basin experienced intrabasinal deformation, uplift and erosion in association with the establishment of external drainage. Fluvial connectivity with the Caspian Sea, however, was interrupted by at least four episodes of basin aggradation. During endorheic conditions the basin fill did not reach the elevation of the plateau interior and hence the Tarom Basin was never integrated into the plateau realm. Furthermore, our provenance data indicate that the northern margin of the basin experienced a greater magnitude of deformation and exhumation than the southern one (IP margin). This agrees with recent Moho depth estimates, suggesting that crustal shortening and thickening cannot be responsible for the vertical growth of the northern margin of the IP, and hence surface uplift must have been driven by deep-seated processes.

KEYWORDS: Iranian Plateau, plateau margin uplift, deep seated processes, magnetostratigraphy, depositional settings, intermontane sedimentation.

1. Introduction

Orogenic plateaus are vast and elevated morphotectonic provinces, which provide the unique opportunity to decipher the interplay between shallow, deep-seated and surface processes, and their influences on Earth's landscape at various timescales (e.g., Dewey et al., 1988; Isacks, 1988; Molnar et al., 1993). They contain internally drained basins that have coalesced and have been filled with thick sedimentary deposits and hence retain insights into orogenic, erosional and geodynamic processes (e.g., Alonso et al., 1990; Meyer et al., 1998; Sobel et al., 2003;, Strecker et al., 2009; Carrol et al., 2010; Horton et al., 2012; Pingel et al., 2019). Plateau's building models predict that reduced fluvial connectivity promotes basin filling, inhibits intrabasinal faulting, and triggers the outward propagation of the deformation fronts. Combined, these processes are thought to be responsible for the lateral (orogen perpendicular) plateau expansion through the integration of new sectors of the foreland into the plateau realm. (Sobel et al., 2003; Garcia Castellanos et al., 2007). The application of these models, however, is not straightforward mostly because the interplay between tectonic and surface processes may trigger different scenarios. This includes basin excavation and erosion with the destruction of the typical plateau morphology (e.g., Strecker et al., 2009; Heidarzadeh et al., 2017). Therefore, while the sedimentary basins in the plateau interior are tectonically stable up to time scales of few 10^7 years (e.g., Alonso et al., 1990; Bush et al., 2016), intermontane basins at the transition with the foreland may experience a more complex evolution including several episodes of basin filling and plateau integration, fluvial incision and tectonic deformation at shorter time scales (10^5 to few 10^6 years; e.g., Streit et al., 2015; Schildgen et al., 2016; Tofelde et al., 2017; Ballato et al., 2019; Pingel et al., 2019). Thus, these transitional basins hold precious information on the

growth of the plateau margin, the evolution of adjacent mountain ranges, the sediment routing systems and the connectivity history among different sedimentary basins.

The NW-SE-oriented Iranian Plateau (IP) is located on the upper plate of the Arabia-Eurasia collision zone and represents the second collisional plateau in elevation and size after Tibet (see Hatzfeld & Molnar, 2010 for a comparison). The IP is parallel to the Zagros orogenic belt and is characterized by high elevation (average elevation is ~1800 m), low internal topographic relief (few hundred of meters), dry climatic conditions, endorheic sedimentary basins in its interior (four out of six basins are internally drained), and steep and dissected flanks bounded by major reverse faults (Ballato et al., 2013, 2017 Heidarzadeh et al., 2017). In central Iran, the northern margin of the IP is marked by a sharp boundary with the adjacent foreland, which comprises the rigid Central Iranian Block (Figure 1). In NW Iran, the IP approaches the Caspian Sea and it is separated from the intracontinental Alborz and Talesh mountains by an elongated, NW-SE oriented intermontane basin called Tarom Basin. Currently, this basin is drained by the Qezel-Owzan River, the second largest river in Iran that flows from the interior of the IP to the Caspian Sea. The basin is composed of post Eocene, synorogenic red beds that offer the opportunity to investigate puzzling aspects of this collision zone, such as: the timing and mechanisms of plateau margin uplift, its lateral expansion (i.e., the possible incorporation of the intermontane Tarom Basin in the plateau realm) and the link with the adjacent growing Alborz Mountains. For this purpose, we have performed a multidisciplinary study including the characterization of the depositional environments, the sediment provenance areas and the depositional age of the post Eocene synorogenic red beds. Our magnetostratigraphic analysis and new zircon U-Pb ages, document that the widespread Eocene arc volcanism terminated at ~ 38-36 Ma, while the deposition of the red beds occurred from ~16.5 Ma to at least ~7.6 Ma during the growth of the

adjacent basin margins. Further, we document the occurrence of alternating periods of efficient and limited fluvial connectivity and we discuss the mechanisms that may have led to the growth of the IP margin in this sector of the Arabia-Eurasia collision zone.

1.1. Geological setting

The Tarom Basin is a NW-SE oriented, elongated, intermontane basin located along the northern margin of the Iranian Plateau between the western Alborz Mountains to the NE and the Tarom range to the SW (Arabia-Eurasia collision zone; Figure 1).

The western Alborz Mountains consist of Pre-Cambrian crystalline basement rocks, Paleozoic and Mesozoic marine deposits, Eocene volcanics, volcaniclastics and intrusives of variable age (Figure 1). This assemblage indicates a complex history of deformation, exhumation, metamorphism, magmatism, subsidence and sedimentation that includes: development of a metamorphic basement during the Neoproterozoic Pan-Africa Orogeny (e.g., Guest et al., 2006; Hassanzadeh et al., 2008), deposition of unconformable carbonate and clastic marine deposits of Pre-Cambrian and Paleozoic age associated with the opening the Paleo-Tethys Ocean (e.g., Horton et al., 2008), occurrence of the Triassic Cimmerian Orogeny (e.g., Zanchi et al., 2009; Omrani et al., 2013), renewed Mesozoic subsidence with the sedimentation of post-orogenic clastic sediments of the Shemshak Formation (e.g., Zanchi et al., 2009; Wilmesen et al., 2009), deposition of shallow- to deep-marine Middle to Late Jurassic sediments during the opening of the South Caspian Basin (e.g., Brunet et al., 2003), Cretaceous thermal subsidence and marine sedimentation (Brunet et al., 2003), Late Cretaceous to Paleocene deformation and exhumation during a regional compressional event (e.g., Guest et al., 2006; Yassaghi & Madanipour, 2008; Madanipour et al., 2017), deposition of Eocene volcaniclastics in a backarc system associated

with the rollback of the Neo-Tethyan oceanic slab (Guest et al., 2006; Ballato et al., 2011, 2013; Verdel et al., 2011; Rezaeian et al., 2012) and finally, contractional deformation and exhumation during the closure of the Neo-Tethys ocean and the collision between Eurasia and Arabia starting from the latest Eocene-earliest Oligocene (e.g., Guest et al., 2006; Ballato et al., 2011, 2013, Rezaeian et al., 2012; Mouthereau et al., 2012; Madanipour et al., 2017, 2018; Pirouz et al., 2017; Koshnaw, et al., 2018). This final event led to development of a narrow, double-verging mountain belt with over 3 km of topographic relief that represents an effective orographic barrier to moist air masses sourced from the Caspian Sea (Figure 1; Ballato et al., 2015). Available low-temperature thermochronology data document slow exhumation from the Early Oligocene followed by an acceleration during the last 12 Ma (Madanipour et al., 2017). Currently, the range accommodates left-lateral shearing between the Caspian Sea and Central Iran (Djamour et al., 2010) and is characterized by the occurrence of few seismogenic faults including the Rudbar Fault, which ruptured in 1990 leading to the catastrophic Mw 7.3 earthquake (Berberian & Walker, 2010). The Tarom range consists of a ~ 4-km-thick pile of Eocene volcanic and volcanoclastic rocks of the Karaj Formation (Figures 1 and 2; Stocklin, J., Eftekharnezhad, J., 1969) that were deposited in the backarc of the Neo-Tethys subduction zone between ~ 55 and 38-36 Ma (Guest et al., 2006; Ballato et al., 2011, 2013; Verdel et al., 2011; Rezaeian et al., 2012). This was associated with the emplacement of Late Eocene (~ 41 to 37 Ma) shallow intrusive rocks (Nabatian et al., 2014). In the Tarom range these deposits form a broad, south-verging anticline (Heidarzadeh et al., 2017) with smaller scales anticline-syncline pairs (Figure 2), cut by minor high angle (both south and north dipping) reverse faults, locally with a lateral component. Available low-temperature thermochronology data indicate that uplift and

exhumation of the Tarom range could have started around the latest Eocene-earliest Oligocene and resumed during the last ~ 10 Ma (Rezaeian et al., 2012).

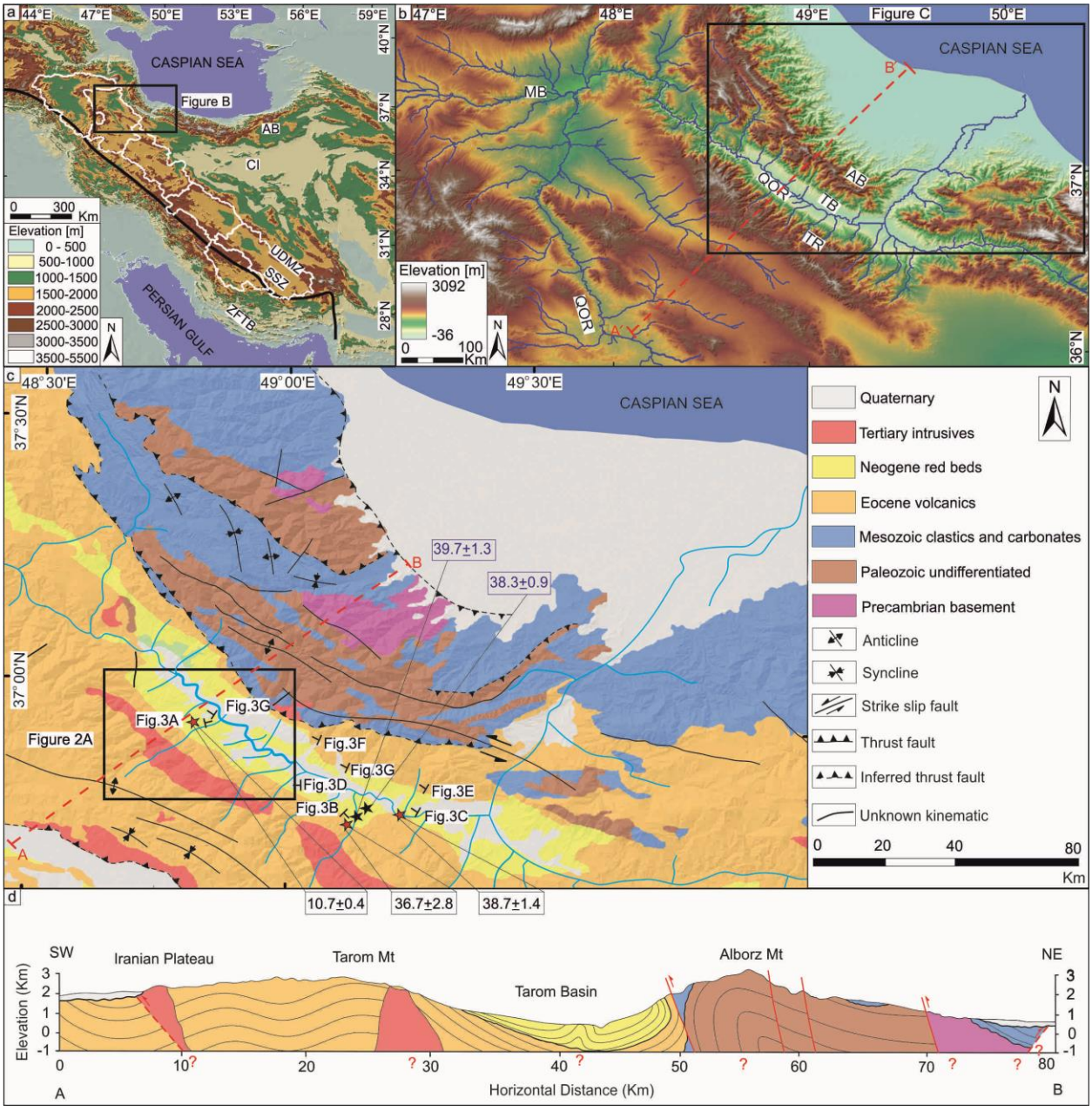

Figure 1. (a) Shuttle Radar Topographic Mission Digital Elevation Model (SRTM DEM) of Iran showing the Iranian Plateau; the white polygons indicate six main drainage basins forming the Iranian Plateau while the black line shows the approximate location of the suture zone, which separates the lower Arabian plate (and the Zagros Fold and Thrust Belt; ZFTB) from the upper Eurasian plate (Ballato et al., 2017). The Urumieh Doktar Magmatic Zone

(UDMZ) and the Sanandaj Sirjan Zone (SSZ) represent the backbones and the margins of the plateau, respectively. (b) DEM of NW Iran showing the Mianeh Basin (MB), Tarom Basin (TB) and its bounding Tarom range (TR) and Alborz Mountains (AB), along the southern and the northern margins of the basin, respectively. Note the Qezel-Owzan River (QOR) drainage system (~ 55000 km^2) connect the Iranian Plateau and the Caspian Sea through the Tarom Basin. A-A´ line shows the approximate location of the crustal scale section shown in figure 14c. (c) Simplified geologic map of NW Iran (Stocklin and Eftekharnezhad, 1969; Davies, 1977) showing the location of the panoramic field photographs of figure 3. The red stars show the location of our new zircon U-Pb ages (expressed in Ma); the black stars (and blue ages) represent reworked Eocene volcanic material within red beds that do not provide information on their depositional age. (d) Regional geological cross section (modified after Stocklin et. al, 1969).

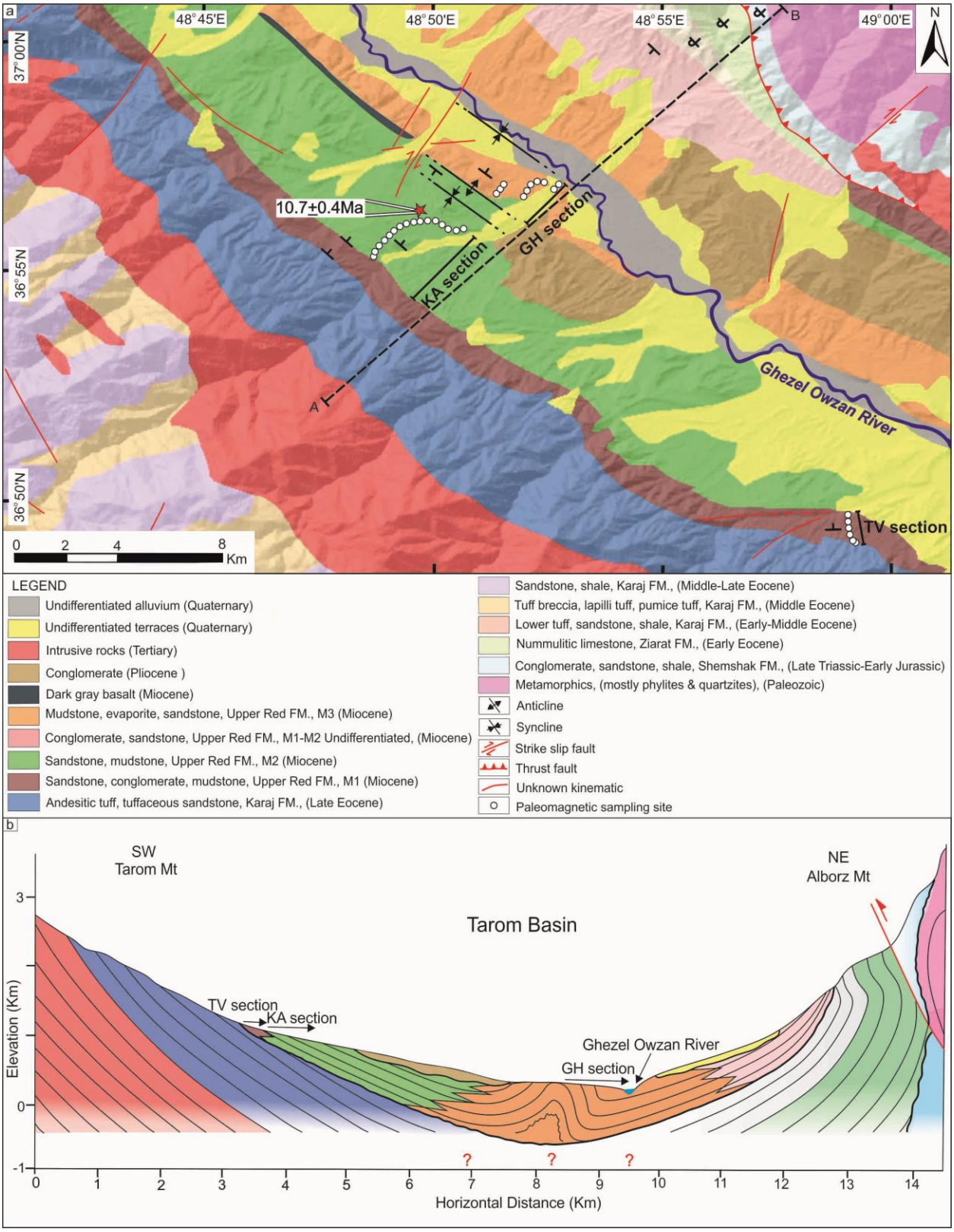
a
48° 45'E
48° 50'E
48° 55'E
49° 00'E
37° 00'N
36° 55'N
36° 50'N
N
A
B
10.7±0.4Ma
KA section
GH section
Ghezel Owzan River
TV section
0 2 4 8 Km
LEGEND
Undifferentiated alluvium (Quaternary)
Undifferentiated terraces (Quaternary)
Intrusive rocks (Tertiary)
Conglomerate (Pliocene)
Dark gray basalt (Miocene)
Mudstone, evaporite, sandstone, Upper Red FM., M3 (Miocene)
Conglomerate, sandstone, Upper Red FM., M1-M2 Undifferentiated, (Miocene)
Sandstone, mudstone, Upper Red FM., M2 (Miocene)
Sandstone, conglomerate, mudstone, Upper Red FM., M1 (Miocene)
Andesitic tuff, tuffaceous sandstone, Karaj FM., (Late Eocene)
Sandstone, shale, Karaj FM., (Middle-Late Eocene)
Tuff breccia, lapilli tuff, pumice tuff, Karaj FM., (Middle Eocene)
Lower tuff, sandstone, shale, Karaj FM., (Early-Middle Eocene)
Nummulitic limestone, Ziarat FM., (Early Eocene)
Conglomerate, sandstone, shale, Shemshak FM., (Late Triassic-Early Jurassic)
Metamorphics, (mostly phylites & quartzites), (Paleozoic)
Anticline
Syncline
Strike slip fault
Thrust fault
Unknown kinematic
Paleomagnetic sampling site
b
SW
Tarom Mt
NE
Alborz Mt
Tarom Basin
TV section
KA section
Ghezel Owzan River
GH section
Elevation (Km)
3
0
-1
0 1 2 3 4 5 6 7 8 9 10 11 12 13 14
Horizontal Distance (Km)

Figure 2. (a) Geologic map (Amini, 1969) superimposed on a SRTM hillshade model of the study area (TB). The white circles show the location of the three sections sampled for magnetostratigraphy named TV, KA and GH. The base of section G is also visible in figure 3h. (b) Geologic cross section across the Tarom Basin.

1.3. Regional stratigraphy

The Tarom Basin was filled by post Eocene red beds that rest in angular unconformity onto Eocene volcanics and volcaniclastics of the Karaj Formation (Figure 2). The stratigraphic position of the red beds is unknown, mostly because the Late Oligocene-Early Miocene marine transgression that led to the widespread deposition of the shallow-water marine limestones of the Qom Formation (Reuter et al., 2009) did not reach the Tarom Basin. These marine deposits are sandwiched between the clastic deposits of the Lower Red (LRF; Oligocene) and Upper Red (URF, Miocene) formations and represent a regional marker that can be followed along the southern margin of the Eurasian plate. Therefore, their absence, does not allow differentiating the stratigraphic position of the red beds exposed in the Tarom Basin, which have been considered either Neogene (Stocklin and Eftekharnezhad, 1969; Davies, 1977) or Miocene in age (Figures 1 and 2; Amini, 1969).

The LRF and the URF are exposed virtually everywhere along the southern margin of the Eurasian plate, where they have a thickness varying from few hundreds to few thousands of meters. These red beds are characterized by a variable amount of sandstones, conglomerates, mudstones, evaporites and locally volcanics, and are mostly considered synorogenic sediments associated with collisional deformation (e.g., Morley et al., 2009; Ballato et al., 2008, 2011, 2017; Rezaeian, et al., 2012; Madaniopour et al., 2017). Lithologically, the LRF is rather heterogeneous, while the URF seems to have more uniform characteristics, and hence has been differentiated into 3 Units (M1, M2 and M3; e.g., Davoudzadeh et al., 1997). Units M1 and M3

183 are generally dominated by mudstones and evaporites with a variable amount of sandstones and
184 conglomerates while Unit M2 is characterized by abundant sandstones. The URF is superseded
185 by supposed Pliocene conglomerates (Hezadarreh Formation; Rieben et al., 1955) that are
186 generally thought to mark an intensification of collisional deformation (e.g., Rezaeian, et al.,
187 2012; Madaniopour et al., 2017). These conglomerates, however, are diachronous and their age
188 depends on their position with respect to the coeval active mountain fronts. For example, in the
189 southern Alborz Mountains (Ballato et al., 2008) and in the interior of the Iranian plateau (Tavaq
190 Conglomerates, Great Pari Sedimentary Basin; Ballato et al., 2017) conglomeratic deposition
191 started at ~ 7.5 and ~ 10.7 Ma, respectively.
192
193 **1.4. Stratigraphic and structural setting of the Tarom Basin**
194 The red beds of the Tarom Basin consist of coarse- to medium-grained clastic deposits passing
195 laterally toward the basin axis to finer grained sediments and evaporites (Figure 3b). The
196 minimum thickness of the basin-fill sediments observable in the field in the central sectors of the
197 basin is about 1185 m, while the lack of major intrabasinal unconformities within the red beds
198 suggests that sedimentation was rather continuous. In some parts, the red beds are
199 unconformably covered by gently deformed, conglomerates of supposed Pliocene age (Figure
200 3a). Furthermore, at least three generations of terrace conglomerates can be observed in the field,
201 suggesting the occurrence of recent phases of sediment aggradation and fluvial incision (Figure
202 3g).
203 Along the southern margin of the basin, the red beds dip few degrees toward the NE (up to 20°),
204 while the underlying volcanics are generally steeper (Figure 3c) and can be locally folded
205 (Figure 3b). In addition, the southern margin of the basin is characterized by several subvertical

synsedimentary normal faults (Figure 3d), mostly parallel to the strike of the basin, that provide evidences for localized extension sub-parallel to the regional shortening direction (NE-SW; Madanipour et al., 2017). These faults are not linked to major extensional events and hence did not control the basin-scale subsidence pattern (Paknia, 2019; PhD thesis; see chapter III).

Along the northern side of the basin, the setting is more variable and complex, and the Eocene deposits of the Karaj Formation are either sub-vertical or overturned. In the central-southern sectors of the basin, the unconformable red beds are also subvertical to overturned (Figure 3e) and exhibit a rapid shallowing upward trend suggesting the occurrence of growth strata. Conversely, in the central-northern sectors of the basin the angular unconformity is more pronounced, and the red beds dip less than 30° to the south-west (Figure 3f). There, we do not have evidences for syndepositional contractional deformation.

The central sectors of the basin are also characterized by several upright syncline-anticlines pairs, subparallel to the strike of the basin with a lateral extent of few kilometers (Figure 2). Figure 3h shows the core of one of these anticlines which is characterized by evaporites layers that have been deformed in a disharmonic manner and may have acted as local decollement horizon.

Currently, the basin is drained by the ~800 km long Qezel-Owzan River (QOR), which is flowing from the elevated Iranian Plateau to the Caspian Sea (Figure 1). The connection between the interior of the Iranian Plateau, the Tarom Basin and the Caspian Sea occurs through a serious narrow bedrock gorges suggesting a protracted history of internal drainage conditions followed by fluvial captures (Heidarzadeh et al., 2017). In particular, the connectivity between the Tarom Basin and the Iranian Plateau must have been established during the last 4 Ma through lake

228 overspill as suggested by the stratigraphic record of a sedimentary basin in the plateau interior
229 (Mianeh Basin, Figure 1b; Heidarzadeh et al., 2017).
230
231
232

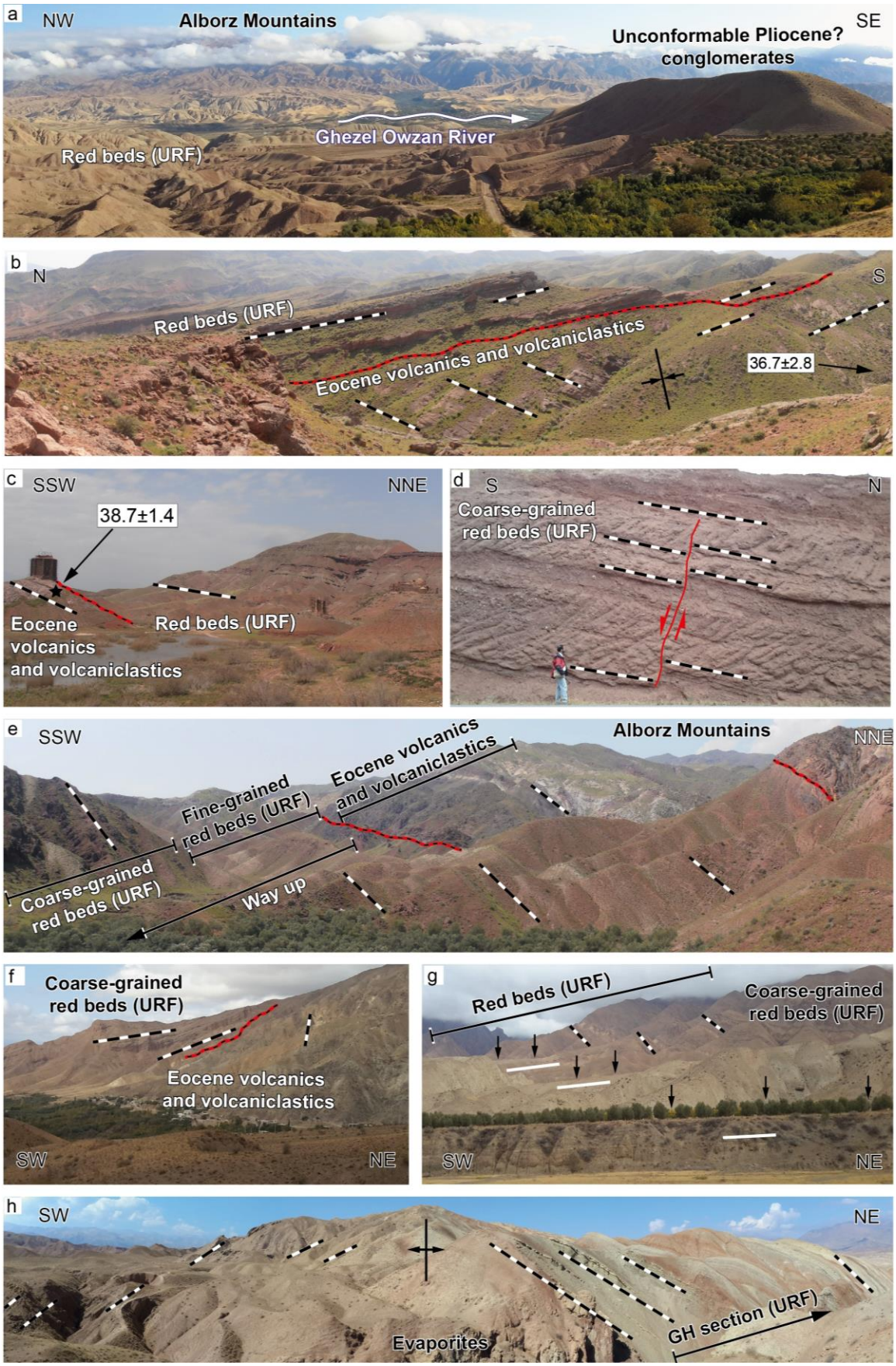
a
NW
Alborz Mountains
SE
Unconformable Pliocene?
conglomerates
Ghezel Owzan River
Red beds (URF)
b
N
S
Red beds (URF)
Eocene volcanics and volcaniclastics
36.7±2.8
c
SSW
NNE
38.7±1.4
Eocene
volcanics
and volcaniclastics
Red beds (URF)
d
S
N
Coarse-grained
red beds (URF)
e
SSW
Alborz Mountains
NNE
Eocene volcanics
and volcaniclastics
Fine-grained
red beds (URF)
Coarse-grained
red beds (URF)
Way up
f
Coarse-grained
red beds (URF)
Eocene volcanics
and volcaniclastics
SW
NE
g
Red beds (URF)
Coarse-grained
red beds (URF)
SW
NE
h
SW
NE
Evaporites
GH section (URF)

233

Figure 3. Panoramic field photographs (see figure 1 for location) highlighting the main geometrical relationships among the units and formations exposed in the Tarom Basin. (a) Northeast-facing photo showing conglomerates supposed Pliocene age in unconformity onto deformed red beds; the conglomerates are tilted to the NNE and have a dip angle of ca. 25°. On the foreground the mountain front of the Alborz Mountains with several generation of terraces is visible (see figure g for details). (b and c) Southeast- and northwest-facing photos documenting the unconformity (red and black line) between the Karaj Formation and the red beds in the southern margin of the basin. Black and white dashed lines show the bedding while the zircon U-Pb ages reported are in Ma (see Table 3 and figure 1). (d) Synsedimentary normal fault exposed along the TV sections (Paknia, 2019; PhD thesis; see chapter III). (e and f) Northwest-facing photos documenting the unconformity (red and black line) between the Karaj Formation and the red beds in the southern margin of the basin. Note that in figure e the red beds are overturned. (g) West-facing photo displaying three major terrace conglomerates (see black arrows); these deposits are virtually undeformed (white lines) and cover in unconformity steeply dipping red beds (black and white dashed lines). (h) Northwest-facing photo showing the core of the anticline that represents the base of the stratigraphic section GH.

2. Material and methods

To unravel the basin-fill history of the Tarom Basin and its tectono-stratigraphic evolution in the framework of collisional deformation and plateau building processes, we performed a multidisciplinary study including:

1) A detailed sedimentologic analysis that provides the basis for an assessment of the depositional environments (Tables 1, 2 and 3; see section 3)

2) A geochronologic study (U-Pb on zircons) of the uppermost volcanic of the Karaj Formation and the red beds that combined with (see section 4)

3) A paleomagnetic and magnetostratigraphic analyses provides a chronostratigraphic framework for the Late Cenozoic basin-fill sediments (see section 4)

4) A provenance study (sandstone petrography and paleocurrent analysis; see section 4), which allows identifying compositional variations related to the exposure of new sediment sources and/or drainage-pattern reorganizations in the sediment source area (Detailed information about the analytical methods are provided in the Appendix section). This approach was employed on two stratigraphic sections exposed along the southern margin of the basin (TV and KA sections; Figure 2) and on a third one located in the northern limb of a north-vergent anticline in the central sectors of the basin (GH section; Figure 2). These sections are stratigraphically continuous and are not affected by major faults, therefore they represent an ideal setting for magnetostratigraphic sampling. Furthermore, recent papers from Central and Northern Iran have shown that the Late Cenozoic red beds have good magnetic properties and hence are suitable for paleomagnetic analysis (Ballato et al., 2008, 2017; Cifelli et al., 2015; Mattei et al., 2015, 2017, 2020). The red beds exposed along the southern basin margin (TV and KA section) are tilted northward with a dip angle of 14 to 30^{o}, whereas in the central sectors of the basin (GH section) strata are steeply dipping to the north (and occasionally overturned) with a dip angle of 40 to 88^{o}. The stratigraphic sections along the southern margin cover the lowermost stratigraphic interval of the basin fill and consist mainly of reddish or light brownish conglomerates with intercalations of mudstone and fine-grained sandstone layers evolving up section into channelized sandstones with conglomerate lenses (fluvial channels, see next section) and finer-grained sediments with tabular geometries (flood plain deposits, see next section). The stratigraphic section in the central sectors of the basin consists mainly of reddish, greyish and brownish mudstones, thin bedded sandstones and evaporates layers, locally with intercalations of conglomerates lenses, which become more abundant toward the top of the section.

3. Depositional systems in the Tarom Basin

Based on our field observations (lithological characteristics, lateral and vertical grain size variations, sedimentary structures and geometry of the sedimentary bodies) and according to the classification scheme of Miall (1985; 1996), we established a total of eighteen lithofacies types (Table 1 and Figure 4) and recognized eight facies associations (Table 2 and Figure 5). The combination of the facies associations led to the reconstruction of four depositional environments (alluvial fan, braided river, playa-lake and lacustrine settings; Figure 5). In the following, we describe the main characteristics of these depositional settings.

3.1. Alluvial fan system

Alluvial fan deposits (Figures 5a and 5b) are located along both margins of the Tarom Basin and include two facies associations: (1) disorganized granule-boulder conglomerate (G1; Figures 4a and 5a), and (2) moderately to well organized granule-boulder conglomerate (G2; Figures 4b and 5b). We interpret the G1 facies association with weakly developed clast imbrications and erosive basal contacts as high-energy stream-floods equivalent to those produced by gravel-laden streams or sediment gravity flow deposits (hyperconcentrated and turbulent flow) in poorly confined channels (Figure 4a and 5a; e.g., Maizels, 1989; Stanistreet & McCarthy, 1993; Ridgway & DeCelles, 1993; Miall, 1996; Blair, 1999). The beds geometry suggests the occurrence of sheet flows (Hein, 1982) with limited development of longitudinal bars (Boothroyd & Ashley, 1975; Todd, 1989). The G2 facies association is interpreted as traction-current deposits in poorly confined channels under conditions of higher bed shear stress (Figures 4b and 5b; e.g., Stanistreet and McCarthy, 1993; Miall, 1996; Blair, 1999; Ballato et al., 2011).

3.2. Braided fluvial system

The braided river deposits (Figures 5c, 5d and 5e) are characterized by four facies associations: (1) well-organized granule-pebble conglomerate (G3), (2) sandstone (S), (3) interbedded fine-grained sandstone and mudstone (SM), and (4) evaporite (E). The G3 facies association is interpreted to reflect traction-current deposits (longitudinal bars or lag deposits) related to the waning stage of high-energy flow in a laterally confined system (e.g., Stanistreet & McCarthy, 1993; Miall, 1996; Blair, 1999). The erosive basal contact, together with the lens geometry and the interfingering with stratified sandstones suggests deposition in a braided channel with a variable proportion of gravel and sand (Figures 4c and 5c; e.g., Miall, 1996). The S facies association is interpreted to represent deposition in lower and upper plane-bed flow regimes in a confined flow (e.g., Miall, 1996). Planar (Sp) and trough cross-stratified (St), medium to coarse-grained, pebbly sandstones are interpreted as migrating bedforms (fluvial dunes) in a confined flow in an upper to lower flow regime (Figure 4c; Uba et. al, 2005; Siks & Horton, 2011). Overall, these observations indicate deposition in fluvial channel. The SM facies association (Figure 5d) includes sandstones with cross (Sr; Figure 4d) and planar lamination (Sh and Sl; Figure 5d) that are interpreted as sheet-flow deposits in a poorly confined to unconfined flow evolving from the upper flow regime to a waning flow stage. The SM facies association includes also massive to parallel laminated mudstones (Fm and Fl; Figure 4f), which can be locally dominant and are interpreted to represent suspension fallout deposits (e.g., Ghibaudo, 1992) from standing or slowly moving waters in the floodplain (e.g., Miall, 1977 and 1978). Locally, the SM facies association are characterized by the development of carbonate nodules and rizholithes indicating paleosols formation (Figure 4g) during lengthy pauses in sedimentation or slow sedimentation rates (e.g., Kraus, 1999). The occasional occurrence of E facies association (Ev;

Figure 4h) is interpreted to represent precipitation of salt minerals from concentrated water solution after evaporation of standing water in the floodplain. Complete desiccation of standing water is also documented by mud cracks (e.g., Lowenstein & Hardie, 1985).

Finally, in the KA stratigraphic section in proximity of the southwestern basin margin we found, embedded in the fluvial deposits, the BD facies association. This disorganized package of blocks with different size and sediments of variable grain size is interpreted as landslide deposits (sturzstrom) caused by gravitational collapse of the adjacent mountain front (e.g., Hermanns & Strecker 1999; Paknia, 2019; PhD thesis; see chapter III, see also Table 2 this work). This interpretation is further supported by the occurrence of a clay-reach sheared basal contact and the presence of a dense and irregular network of fractures (jigsaw cracks).

3.3. Lacustrine system

The lacustrine system is located along the central sectors of the basin (Figures 4e, 4f, 5f and 5f; section GH) and is characterized by two facies associations: (1) mudstone (M) and (2) interbedded fine-grained sandstone and mudstone (SM). Tabular bodies of laminated mudstone of the M facies association are typical of suspension deposits in a lacustrine offshore setting and indicate a deepening of the system (Figure 4f). Lenses of fine grained-sandstone with symmetrical ripple marks interbedded with mudstone (lenticular and waving bedding Figures 4e and 5f) in the SM facies association indicate deposition in the lacustrine shoreface-offshore transition. In few sectors of the GH stratigraphic section, the tabular sandstones with symmetric ripples become dominant suggesting sedimentation in the lacustrine shoreface (e.g., Horton & Schmitt, 1996; llgar & Nemec, 2005; Chakraborty & Sarkar, 2005; Keighley, 2008; Ghinassi et al., 2012). These intervals, however, are relatively rare and generally have a limited thickness (<

1 m), therefore most of the lacustrine sediments exposed in the section were deposited either in the offshore or in the shoreface-offshore transition setting.

3.4. Playa lake system

The playa lake system is also located in the central sectors of the basin where it alternates with the lacustrine setting (GH stratigraphic section, Figures 4h and 5h). These deposits include two facies associations such as (1) mudstone (M) and (2) evaporite salt minerals (E). The first facies association (mudstone; M) is interpreted to represent deposits settled from suspension in arid to semiarid, oxidizing conditions as documented by the presence of red coloured sediments and the occurrence of desiccation cracks (e.g., Lowenstein & Hardie, 1985). The second facies association (E) is interpreted to represent evaporite layers (mostly gypsum) precipitated during short-lived rain episodes followed by desiccation. Overall, these observations suggest that sedimentation occurred in a shallow playa lake setting.

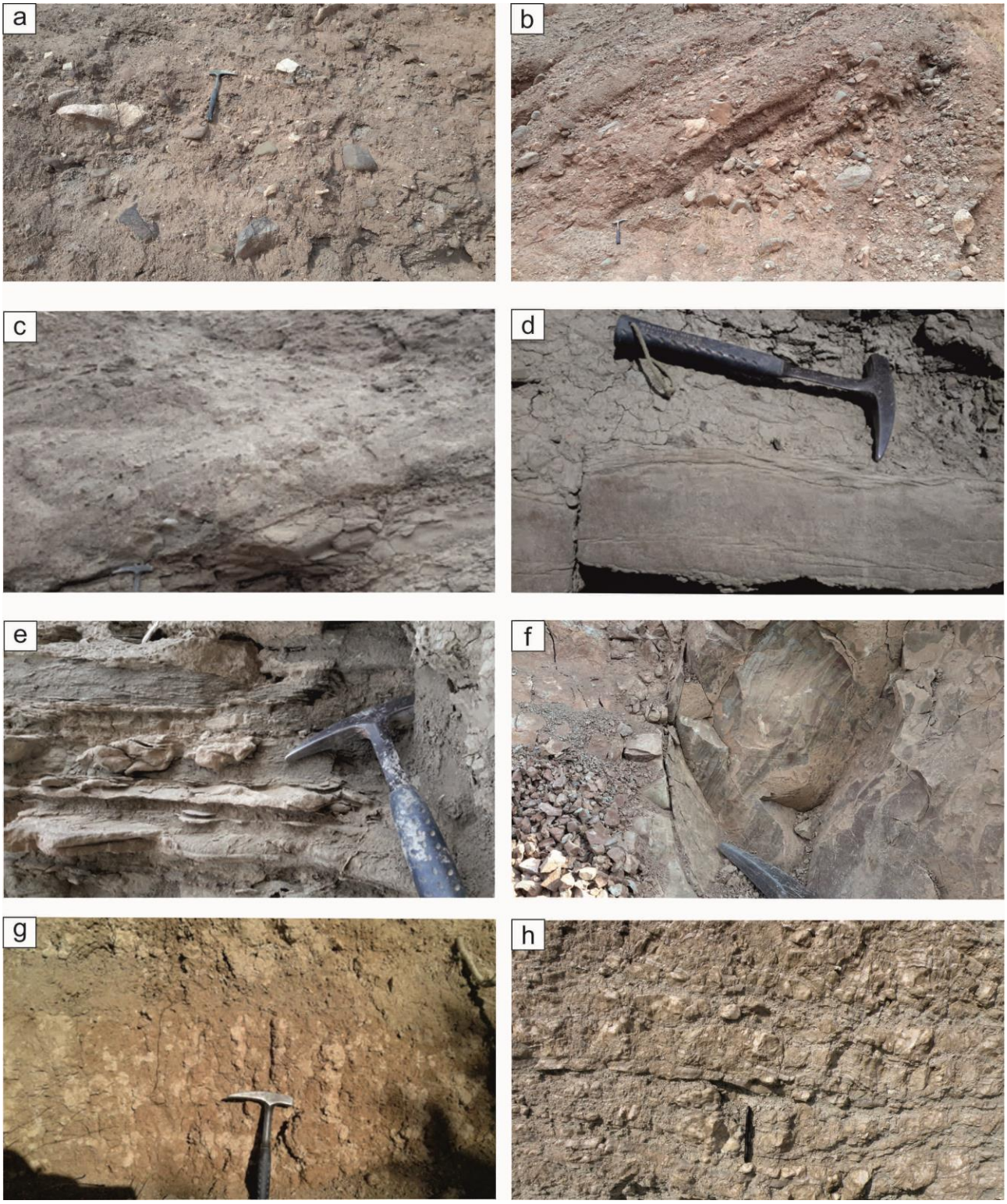

Figure 4. Close up view photographs of lithofacies characteristics. (a) Disorganised, structureless, matrix-supported, mostly monomictic (clasts are Eocene volcanics) conglomerate with subangular to angular clasts reflecting mass flow deposits (Facies code Gmd). (b) Disorganised, structureless, clast-supported, mostly monomictic conglomerate

with crude bedding and subangular to moderately rounded clasts (stream-flood deposits; Gcd). (c) Conglomerates and coarse-grained sandstones with planar cross bedding representing traction current bedforms (Gp and Sp, respectively). (d) Horizontally laminated sandstone (Sl) and rippled sandstone (Sr) indicating traction currents of variable energy in sandy dominated system. (e) Lenticular bedding with symmetrical rippled sandstone (Smw) alternated with laminated mudstone (Fl) reflecting an alternation of current (bidirectional) and suspension deposits. (f) Massive structureless (Fm) to finely laminated (Fl) calcareous mudstone (suspension deposits). (g) Mudstone with carbonate nodules (P) indicating paleosol formation. (h) Evaporate deposits (Ev) reflecting evaporation from standing water.

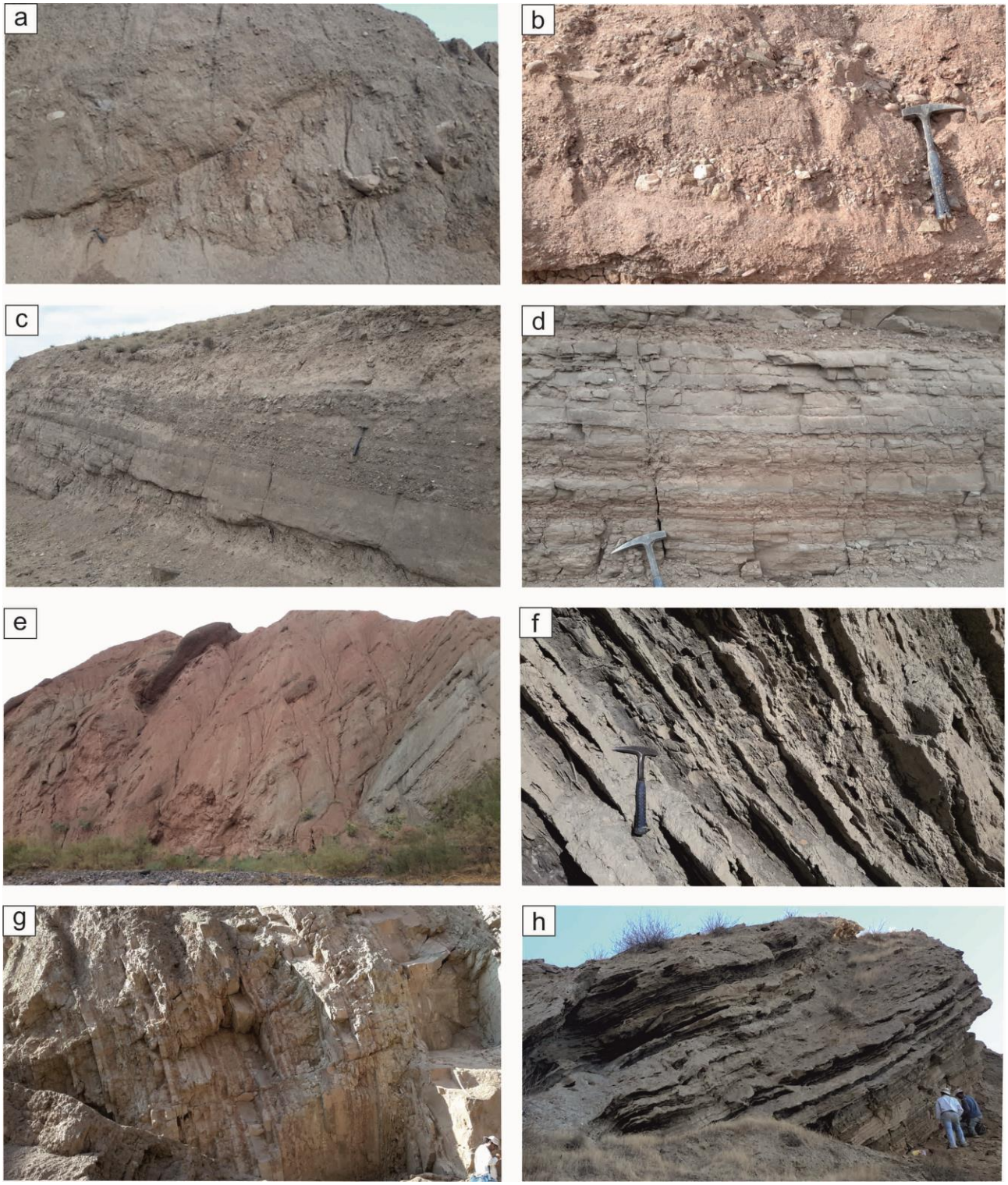

Figure 5. Representative views of different depositional systems in the Tarom Basin. (a) Disorganized granule-boulder conglomerate (facies association G1; base of KA stratigraphic section) and (b) moderately to well organized granule-boulder conglomerate (facies association G2; KA stratigraphic section) representing an alluvial fan setting.

384 (c) Horizontally to trough cross-stratified pebbly sandstone and conglomerate in a fluvial channel (facies association
385 S; KA stratigraphic section), of a braided river system. (d) Horizontally, thin bedded, fine grained sandstone and
386 laminated mudstone sheets (facies associations SM; KA stratigraphic section) representing flood plain deposits of
387 the braided river system. (e) Overview of the braided river system with lenses of conglomerate and coarse-grained
388 sandstone (facies association S and G3) embedded in flood plain deposits (facies associations SM; top of GH
389 stratigraphic section). (f) Fine grained sandstone and mudstone deposits with flat geometry (facies association SM;
390 GH stratigraphic section) reflecting deposition in the shoreface-offshore transition in a lacustrine depositional
391 setting; the sandstone layers indicate distal storm beds. (g) Alternation of mudstone and fine-grained sandstone
392 deposit with flat to tabular geometry (facies association SM; base of GH stratigraphic section; lacustrine
393 depositional setting); when the mudstone dominates deposition occurred in the offshore setting, otherwise the
394 alternation of mudstone and sandstone indicates deposition in the shoreface-offshore transition. (h) Gypsum layers
395 (Evaporite deposits) precipitated during short-lived desiccation episodes (facies association E, GH stratigraphic
396 section), representing a playa lake depositional setting.
397
398 **Table 1**
399 *Description and Interpretation of Lithofacies*

Facies code	Characteristics	Interpretation
Gmd	Disorganised, structureless, matrix-supported, mostly monomictic conglomerate. Granules to boulders, subangular to angular clasts. Maximum clast diameter 40 cm	Mass flows deposits from hyperconcentrated or turbulent flow
Gcd	Disorganised, structureless, clast-supported, mostly monomictic conglomerate with crude bedding. Granules to boulders, subangular to moderately rounded clasts. Maximum clast diameter 40 cm	Stream-floods deposits with concentrated clasts
Gco	Moderately organized, clast supported, monomictic to polymictic conglomerate. Granules to cobbles, subangular to rounded clasts, normal grading, and weak imbrication. Maximum clast diameter 20 cm	Traction bedload deposits
Gh	Clast-supported, horizontally bedded, monomictic to polymictic conglomerate. Granules to pebbles, subrounded to well-rounded clasts, normal to inverse grading with imbrication. Maximum clast diameter 5 cm	Traction current bedforms (bars)

Gt	Clast-supported, trough cross-stratified, monomictic to polymictic conglomerate. Granules to pebbles, subrounded to well-rounded clasts, normal grading. Maximum clast diameter 5 cm	Traction current bedforms (bars)
Gp	Clast-supported planar cross-stratified monomictic to polymictic conglomerate. Granules to pebbles, subrounded to rounded, normal grading. Maximum clast diameter 5 cm	Traction current bedforms (bars)
Br	Matrix supported, structureless monomictic breccia. Granules to boulders, very angular clasts, inverse grading. Maximum clast diameter 1 m	Rock avalanche deposits (sturzstrom)
Sp	Planer cross-stratified sandstone. Medium to coarse grain size, moderately to well sorted occasionally with pebbles	Dune migration during upper to lower flow regime
Sl	Horizontally laminated sandstone. Very fine to medium grain size, well sorted occasionally with pebbles	Bedforms deposited under upper to lower flow regime
Sr	Rippled sandstone (asymmetric ripples). Very fine to medium grain size, well sorted	Ripples under lower flow regime
Sh	Horizontally stratified sandstone. Very fine to coarse grain size, moderately to well sorted, occasionally with pebbles	Planar bed flow during upper flow regime
St	Trough cross-stratified sandstone. Medium to coarse grain size moderately to well sorted, occasionally with pebbles	Dune migration during upper to lower flow regime
Smw	Rippled sandstone (symmetrical ripples). Fine to medium-grain size well sorted	Wave (bidirectional current) deposits
Fm	Massive structureless calcareous mudstone	Suspension deposits, overbank or abandoned channel
Fl	Finely laminated calcareous mudstone. Flat parallel lamination, small-scale ripples, locally with mud cracks	Suspension deposits, overbank or abandoned channel
Mr	Sheared reddish clay with unsorted angular clasts	Shearing stress at the base of a rock avalanche
P	Mudstone to fine-grained sandstone with carbonate nodules	Paleosol formation
Ev	Evaporites, locally associated with gypsum-filling fractures	In situ accumulation during evaporation of standing water

400

401

402 **Table 2**

403 *Description, Lithofacies, Architectural Elements, and Interpretation of Depositional Processes and Environments of*

404 *Facies Association*

Facies association	Description	Lithofacies	Architectural elements	Interpretation of depositional process	Depositional setting
G1 (disorganized granule-boulder conglomerate)	Structureless to poorly organized, matrix- to clast-supported conglomerate. Beds 0.2 to1 m thick with lateral extent of few tens of meters and a planar to slightly erosive basal contacts. Interbedded with facies associations G2 and G3	Gmd, Gcd	Gravel sheets and poorly confined channels	Sediment gravity-flow deposits	Alluvial-fan system
G2 (moderately to well organized granule-boulder conglomerate)	Moderately to well-organized, clast-supported, ungraded to normally graded, moderately to poorly sorted, poorly imbricated conglomerate. Moderate to poor horizontal and trough cross-stratification. Beds 0.2- to 1-m-thick with a lateral extent of few tens of meters and a slightly erosive basal contact. Interbedded with facies associations G1, G3, S and SM	Gco, Gh, Gt	Gravel sheets, and gravel downstream accretion macroforms (bars)	Traction bedload deposits in a gravel-dominated, poorly confined channel or in a gravel sheet	Alluvial-fan system
G3 (well organized granule-cobble conglomerate)	Well organized, clast-supported, channelized, horizontally, planar and trough cross-bedded, moderately to well sorted, conglomerate with slightly erosional contacts and a lateral extent of up to tens of meters. Interbedded with facies associations S, G2, SM, and rarely M	Gco, Gp, Gh, Gt, Sh, St, Sp	Channel-fill complex and gravel bedforms (gravel bars and lenses)	Traction bed load deposits in a gravel-dominated, well-confined channel	Alluvial-fan and proximal fluvial system
DB (Disorganized, granules to boulder breccia)	Chaotic, matrix supported, poorly sorted breccia with a sheared clay basal contact and few tens of meters lateral extent	Br, Mr	Probably lobate (full geometry not exposed)	Gravitational collapse from the adjacent mountain front	Landslide deposits (sturzstrom)
S (sandstone)	Channelized, fine to medium-grained, locally coarse-grained to pebbly, normally grained, fining upward sandstone. Sedimentary structures include horizontal, planar and trough cross-bedding and towards the top of the sandstone body ripples and parallal lamination. Beds 0.3-	Sh, St, Sp, Sl, Sr, Gh, Gt, Gp	Channel-fill complex, sandy bedforms and sandy downstream accretionary	Channel fill deposits in a well-confined sand-dominated fluvial channel	Fluvial system (channel complex)

	to 1.5-m-thick with lateral extent of few tens of meters. Erosive concave-up base contacts. Interbedded with facies G3, SM, M, and rarely E		macroforms		
SM (interbedded fine-grained sandstone and mudstone)	Fine-grained sandstone and siltstone with a tabular geometry. Sedimentary structures include parallel lamination symmetrical and asymmetrical ripples locally climbing. Beds 0.1- to 0.5-m-thick, and a lateral extent up to several tens of meters. Basal contacts are flat, non-erosive, and rarely slightly concave up. Proportion between mudstone and sandstone variable. Locally, palaeosol horizons consisting of mottled mudstone and calcite nodules, developed. Interbedded with facies S, G3, M and locally E (in this case they are associated with gypsum-filled fractures)	Sh, Sl, Sr, Smw Fl, Fm, P	Sheet-like and wedging deposits	Sheet-flow deposits in poorly confined to unconfined flow, evolving from upper flow regime to waning flow stage and suspension from standing water, and lacustrine sediments deposited either above the mean fair-weather wave base (sandstone dominating) or above the mean storm wave base (mudstone dominating)	Fluvial (floodplain), playa-lake and lacustrine system (beach to nearshore and offshore environment)
M (mudstone)	Massive to laminated grey to light red mudstone. Locally, poorly developed calcrete as well as gypcrete. Beds with a flat non-erosive contact typically 0.02- to 0.5-m-thick and a lateral extent up to several tens of meters. Interbedded with facies S, SM, and locally E (in this case they are associated with gypsum-filled fractures)	Fl, Fm, P	Sheet-like	Suspension deposits in standing water	Fluvial (floodplain), playa-lake and lacustrine system (offshore)
E (evaporite)	Evaporite deposits, 0.05 to 0.3 m thick with a lateral extent of several tens of meters. Generally associated with gypsum-filled fractures. They can form packages of	Ev	Sheet-like	Evaporation deposits from standing water	Play-lake or fluvial (highly

	up to 20 m. Interbedded with facies M, rarely with SM and S				evaporative flood plain) system

405

406

407 **4. Results**

408 **4.1. Zircon U-Pb geochronology**

409 Five samples were collected for Zircon U-Pb dating in the Eocene volcanics and the Neogene red
410 clastics to constrain the top age of the Karaj Formation and provide independent age constrains
411 on the depositional age of the synorogenic red beds. Results are shown in table 3 and in the
412 Appendix A1.

413 The contact between the Karaj Formation and the overlying red beds is well exposed along both
414 margins of the basin. Considering that the northern margin has experienced a greater degree of
415 deformation and erosion (compare Figures 3b and 3c with Figures 3e and 3f) we sampled the
416 contact along the southern margin of the basin in two different locations (Figure 1). Sample GH-
417 15-03 represents a > 20-m-thick white tuff that can be followed along strike for about five
418 kilometers. This lithotype is stratigraphically located below a thick package (several tens of
419 meters) of coarse-grained volcaniclastic deposits that are less suitable for zircon U-Pb dating and
420 represent the top of the Karaj Formation in this area (Figure 3b). These units are characterized by
421 a system of open syncline-anticline pairs with a wavelength of several tens of meters (Figures 3b
422 and 6). Our tuff sample (GH-15-03) yielded only few zircon grains with a weighted average age
423 of 36.7 ± 2.6 Ma (Table 3). We collected another sample (GH-15-01) along strike to the SE from
424 a rhyolite exposed on top the Karaj Formation (Figure 3c). In this area the angular unconformity
425 with the overlaying red beds has a low angle (< 10°). This sample yielded a weighted average

age of 38.7 ± 1.4 Ma. This age overlaps with the previous sample (within a two-sigma error) suggesting that the termination of widespread arc volcanism should have occurred sometime between 38 and 36 Ma. This age agrees with those obtained by previous studies (~ 36 Ma, Ballato et al., 2011; ~ 37 Ma, Verdel et al., 2011) in central and northern Iran.

An additional, few cm-thick, ash layer (TM-16-01) was collected within the red beds in proximity of the top of the KA stratigraphic section. This sample is fundamental for pinpointing the magnetostratigraphic correlation (see next sections) and yielded a weighted average age over 13 grains of 10.7 ± 0.4 Ma (Table 3). This value does not include nine grains that clustered around 13-12 Ma. If we include these grains the weighted average age over 22 grains will be 11.3 ± 0.5 Ma (Table 3). Considering that a ~ 10.7-My-old tuff has been dated about 120 km to the NW in three different locations (Ballato et al., 2017), we prefer to consider the 10.7 Ma option as more reliable that the 11.3 Ma. Accordingly, the 13-12-My-old zircon grains should represent crystals that spent 2-3 million of years in the magmatic chamber before the eruption.

Finally, two more samples were collected in the red beds, directly upsection of sample GH-15-03. These two samples are located right above the unconformity (GH-15-02, resampled in a second stage as GH-17-02) and about 400 m (stratigraphically) above it (GH-17-04; Figure 6). The first sample is a weathered, reworked white tuff, while the second one is a light green tuffaceous sandstone with very pristine biotite crystals. These samples gave very similar ages (39.7 ± 1.3 and 38.3 ± 0.9 Ma, respectively; Table 3), which look almost identical to those obtained for the top of the Karaj Formation. Therefore, based on the stratigraphic separation between them we consider these two samples as reworked volcanic material from the eroding Karaj Formation that does not provide indication about the depositional age of the red beds.

448 Combined, our new zircon ages indicate that arc volcanism in this area must have lasted until 38-
449 36 Ma, while the deposition of the red beds appears to have occurred during the Miocene.

450

451 **Table 3**

452 *Zircon U-Pb Dating Results*

Sample code	Age (Ma)	Error 2s (Ma)	N of grains analyzed	N of grains used	MSWD	Rock type	Formation / Unit	Lat (Dec°)	Long (Dec°)	Elevation (m)
GH-15-01	38.7	1.8	11	10	0.4	Rhyolite	Karaj F	36.74525	49.23086	375
GH-15-02/ GH-17-02	39.7	1.3	18	16	1.8	Reworked tuff	Red Beds	36.70804	49.14391	752
GH-15-03	36.7	2.8	6	4	0.8	White tuff	Karaj F	36.70342	49.14172	840
GH-17-04	38.3	0.9	10	10	1.0	Tuffaceous sandstone	Red Beds	36.72139	49.14806	576
TM-16-01	10.7	0.4	24	13	1.3	Ash	Red Beds	36.91298	48.83748	600
TM-16-01 alternative	11.3.	0.5	24	22	3.8					

453

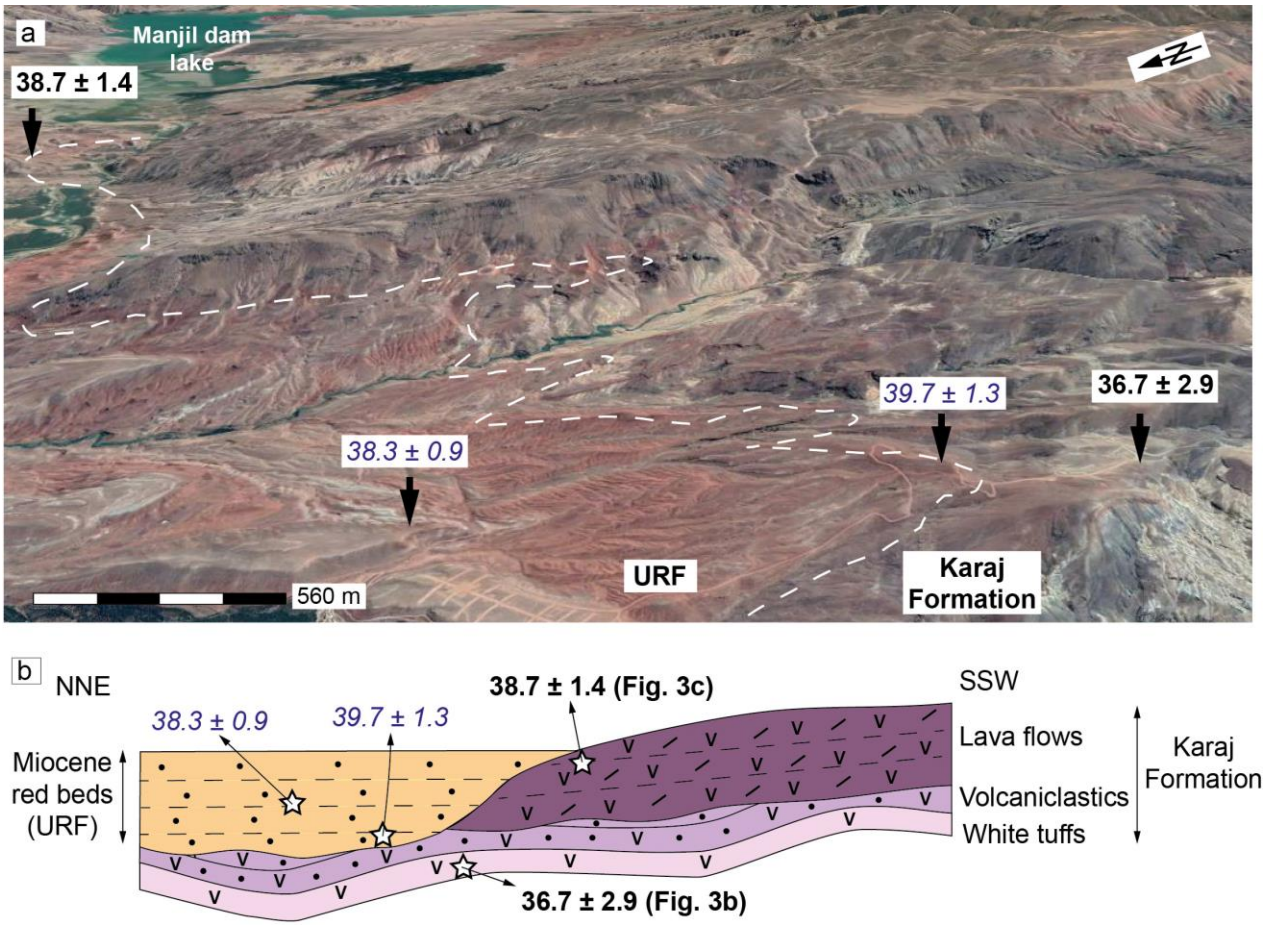

Figure 6. (a) Google Satellite Imagery showing the relationship between the Karaj Formation and the red beds along the southern margin of the basin in proximity of the Manjil dam lake (see the same ages reported figure 1 for location). (b) Schematic cartoon showing the geometrical relationships between the top of the Karaj Formation and the red beds along the southern margin of the Tarom Basin.

4.2. Paleomagnetic results

Seventy-two samples were collected along the 153-m-thick TV stratigraphic section (M1 member), while 143 and 321 samples were collected from the 565-m-thick KA (M2 member) and the 1185-m-thick GH Section (M3 member), respectively. Paleomagnetic sampling was carried out using an ASC 280E petrol-powered transportable drill with a water-cooled diamond bit. Cores were oriented in situ using a magnetic compass. Five hundred thirty-four samples were

466 measured at the Alpine Laboratory of Paleomagnetism (ALP) at Peveragno (Turin) and at the
467 INGV Laboratory of Paleomagnetism (Rome, Italy) shielded room, using a 2G Enterprises DC-
468 SQUID (superconducting quantum interference device) cryogenic magnetometer. Data were
469 analysed using the software Remasoft 3.0 (Chadima & Hrouda, 2006). The NRM of one
470 specimen per core was measured by means of progressive stepwise demagnetization using
471 thermal (384 specimens) or alternating field (AF) (150 specimens) procedures. Thermal
472 demagnetization was carried out using temperature increments (80-100°C up to 430°C and 30-
473 50°C above 430°C) until the NRM decreased below the limit of instrument sensitivity or random
474 changes appeared in the paleomagnetic directions. Stepwise AF demagnetization was carried out
475 using a set of three orthogonal AF coils mounted in-line with the Superconducting Rock
476 Magnetometers (SRM) system, with 5–10 mT increments up to 20 mT, followed by 20 mT steps
477 up to 120 mT.
478 One hundred sixty-two samples were either too weakly magnetized to allow reliable complete
479 stepwise demagnetization or gave unstable directions during stepwise demagnetization. Such
480 samples were discarded from further analyses. In most of the remaining samples, after the
481 removal of a viscous low temperature/low coercivity normal polarity component at 180°/250° C
482 or 10-30 mT, the NRM vectors aligned along a single linear path toward the origin of the
483 orthogonal diagrams for both normal and reverse polarities (Figure 7a-f). In these samples
484 ChRM directions were calculated by principal component analysis (PCA) (Kirschvink, 1980) of
485 the linear component between 250/320°C and 530/660°C.

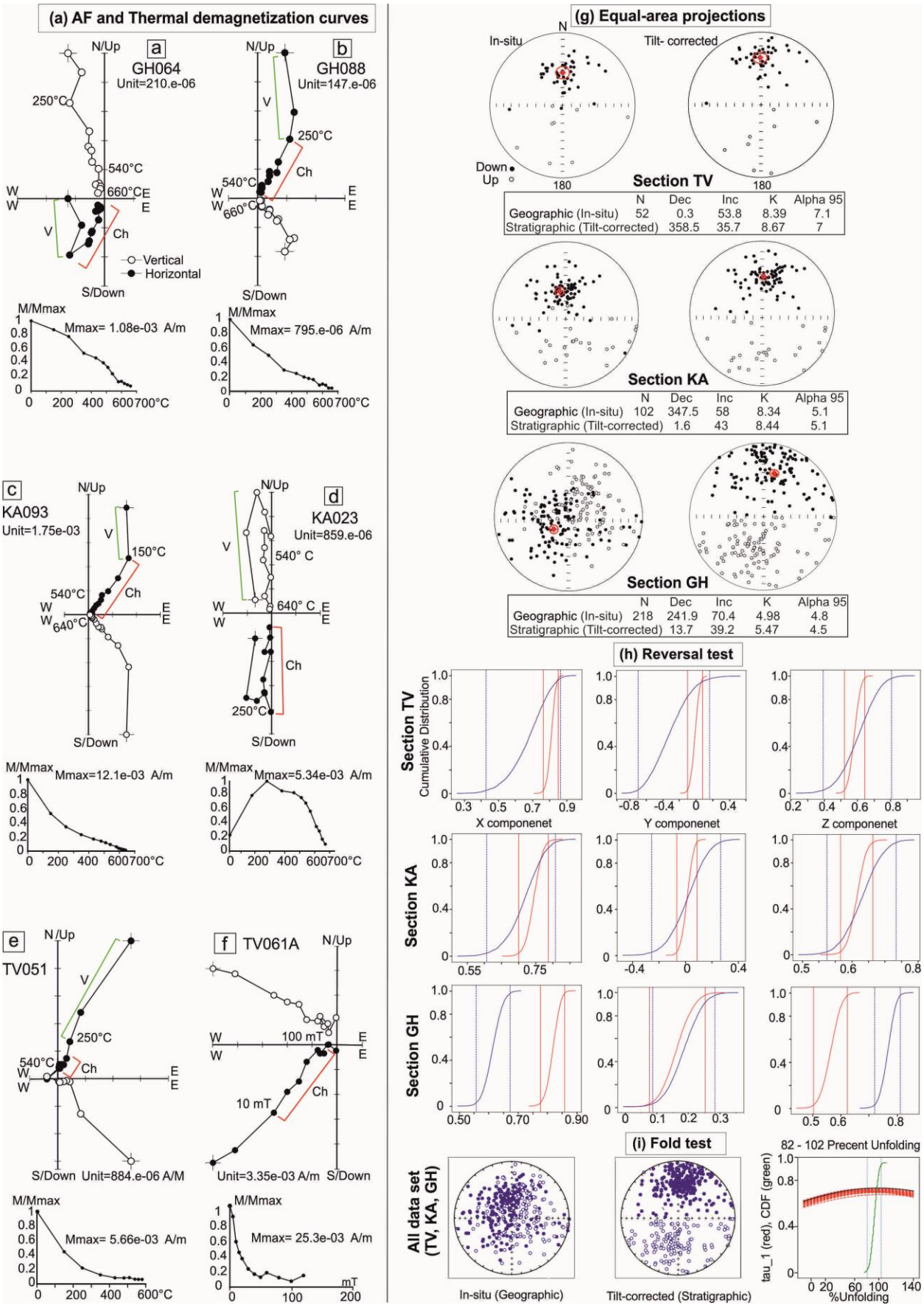

Section TV	N	Dec	Inc	K	Alpha 95
Geographic (In-situ)	52	0.3	53.8	8.39	7.1
Stratigraphic (Tilt-corrected)		358.5	35.7	8.67	7

Section KA	N	Dec	Inc	K	Alpha 95
Geographic (In-situ)	102	347.5	58	8.34	5.1
Stratigraphic (Tilt-corrected)		1.6	43	8.44	5.1

Section GH	N	Dec	Inc	K	Alpha 95
Geographic (In-situ)	218	241.9	70.4	4.98	4.8
Stratigraphic (Tilt-corrected)		13.7	39.2	5.47	4.5

Figure 7. (a) Tilt corrected diagrams of Thermal and AF demagnetization analysis of representative samples. Demagnet ization diagrams and intensity decay curves are shown to the left. The black and white circles represent projections onto the horizontal and vertical plane, respectively (Zijderveld, 1967), while numbers at each demagnetization step denote temperatures in °C (150 to 680) and magnetic field values in mT (5 to 120). (b) Mean normal and reverse polarity of ChRM components for the three investigated stratigraphic sections on equal-area stereographic projection in geographic and tilt-corrected coordinates (Dec = declination; Inc = inclination; K = precision parameter, α95 = semi-angle of the cone of 95% confidence). (c) Bootstrap reversal test results for the three stratigraphic sections and (d) fold test results for the entire dataset (Tauxe et al., 1991). The reversal test on TV and KA samples is positive, while GH samples show a negative reversal test. The fold test (all samples from the three studied sections) is positive.

4.2.1. TV stratigraphic section

In the TV Section the initial Natural Remnant Magnetization (NRM) intensities vary between 8.59×10^{-4} and 1.01×10^{-2} A/M (Figure 8). The highest NRM values (average of 4.34×10^{-2} A/M) were obtained in the alluvial fan deposits at the base of the section (first ~15 m; Figure 8). The bulk susceptibility (k) values range from 170 to 10970×10^{-6} SI (Figure 8). High k values are most probably related to the significant contribution of the volcanoclastic Karaj Formation which is particularly rich in magnetite (Ballato et al., 2008). In the TV Section a reliable ChRM has been obtained in 54 samples, 8 with a reverse polarity and 45 with a normal polarity. The maximum angular deviation (MAD) of the recognized magnetic components is lower than 10° (52 samples) except for two samples where it is 11.2 and 14.9°.

4.2.2. KA stratigraphic section

In the KA Section the initial Natural Remnant Magnetization (NRM) intensities vary between 9.91×10^{-4} and 1.01×10^{-2}A/M, whereas the bulk susceptibility (k) values range between 460

and 26570 × 10^{-6} SI (Figure 9). As for the TV Section these high values are probably related to the presence of detrital magnetite from the Karaj Fm. In the KA Section a reliable ChRM has been obtained in 102 samples, 25 with a reverse polarity and 77 with a normal polarity. The maximum angular deviation (MAD) of the recognized magnetic components is lower than 10° in 85 samples and it varies between 10.2 and 14.8° in 18 samples.

4.2.3. GH stratigraphic section

NRM intensities for the GH samples are about one order of magnitude lower than the other two sections, and vary between 9.89 × 10^{-5} and 1.01 × 10^{-3} A/M (Figure 10). Magnetic susceptibility (k) values are also lower than those recorded in the other sections, and range from 70 to 3650 × 10^{-6} SI, possibly reflecting a more composite sediment source area (Figure 10). In the GH Section a reliable ChRM has been obtained in 218 samples, 98 with a reverse polarity and 120 with a normal polarity. The maximum angular deviation (MAD) of the recognized magnetic components is lower than < 10° in 200 samples and is comprised between 10.1 and 14.8° in 18 samples.

537

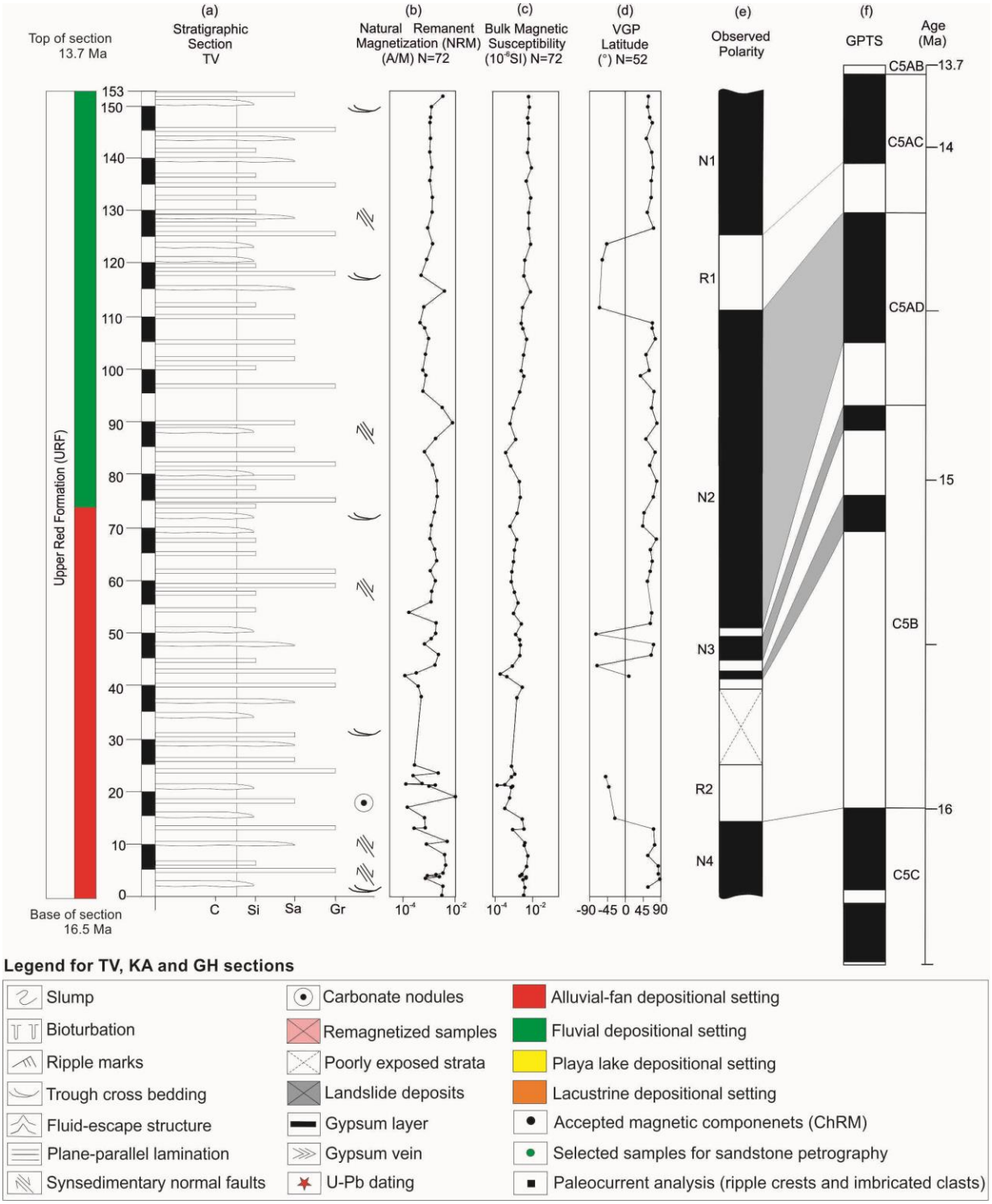

538

539 Figure 8. (a) Stratigraphic sections TV including (b) NRM (Natural Remnant Magnetization), (c) Bulk magnetic

540 susceptibility, and (d) VGP latitude (Virtual Geomagnetic Pole). The VGP latitudes were used for constructing (e)

observed polarity scales, which were subsequently correlated each stratigraphic section with (f), the reference GPTS (geomagnetic polarity time scale) of Gradstein et al. (2012). Grey magnetozones of observed polarity scale were detected by means of only one sample

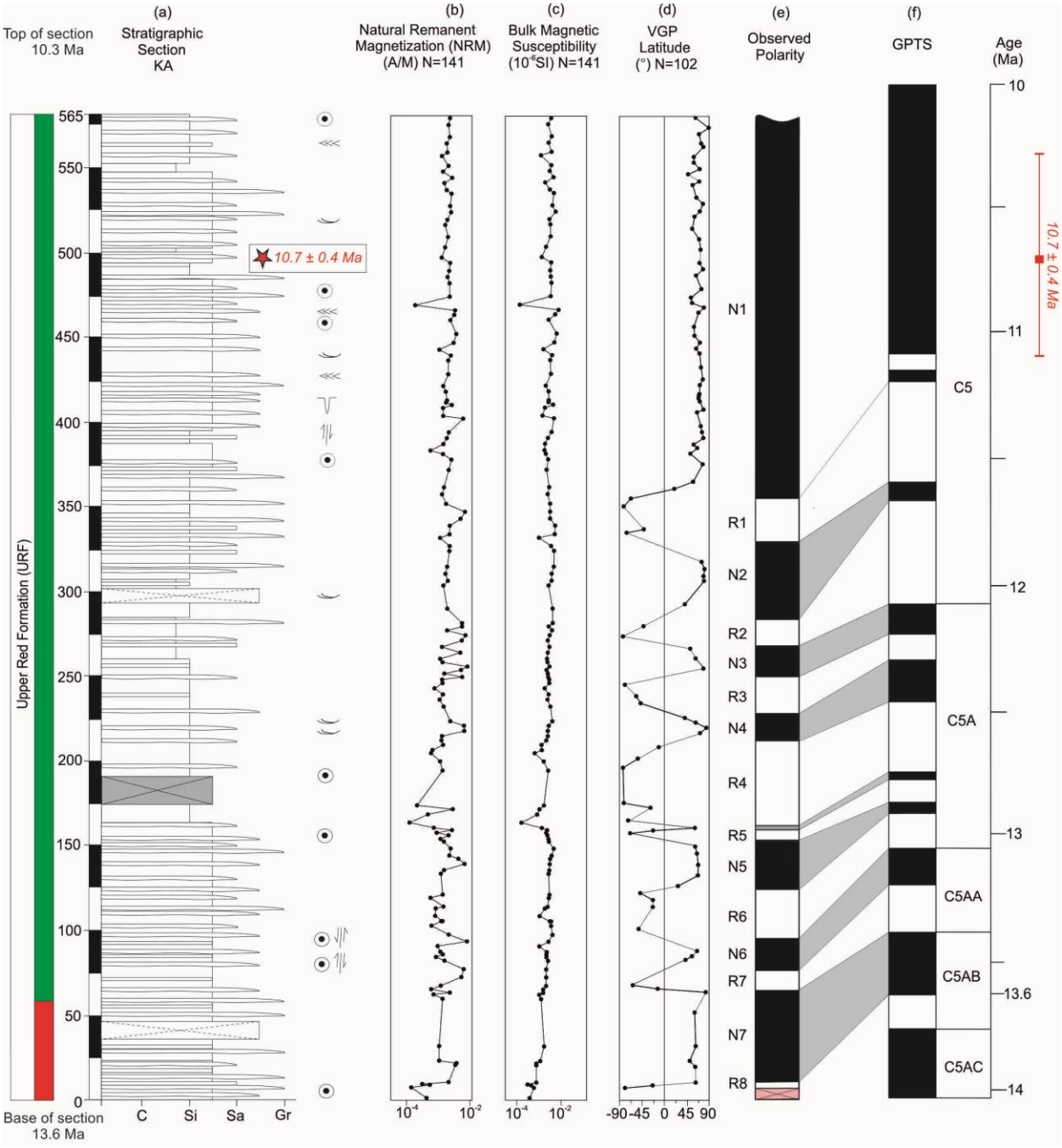

Figure 9. (a) Stratigraphic sections KA including (b) NRM (natural remnant magnetization), (c) Bulk magnetic susceptibility, and (d) VGP latitude (virtual geomagnetic pole). The VGP latitudes were used for constructing (e) observed polarity scales, which were subsequently correlated each stratigraphic section with (f), the reference GPTS

548 (geomagnetic polarity time scale) of Gradstein et al. (2012). Grey magnetozones of observed polarity scale were
549 detected by means of only one sample.

550
551

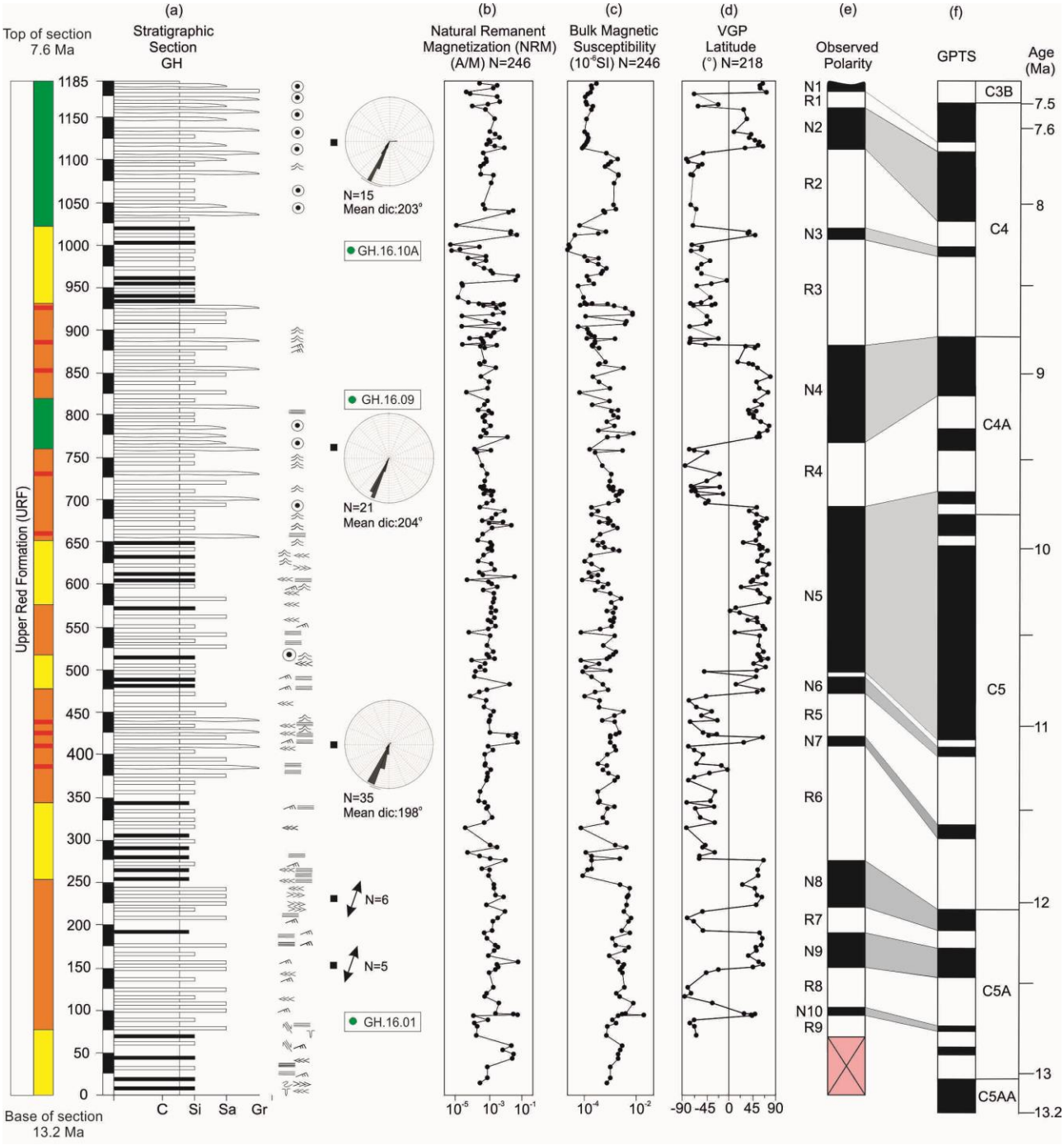

552

553 Figure 10. (a) Stratigraphic sections GH including (b) NRM (natural remnant magnetization), (c) Bulk magnetic
554 susceptibility, and (d) VGP latitude (virtual geomagnetic pole). The VGP latitudes were used for constructing (e)

555 observed polarity scales, which were subsequently correlated each stratigraphic section with (f), the reference GPTS
556 (geomagnetic polarity time scale) of Gradstein et al. (2012). Grey magnetozones of observed polarity scale were
557 detected by means of only one sample
558
559 **4.2.4. Paleomagnetic tests**
560 To assess the primary nature of the isolated ChRM directions the reversal and fold tests were
561 performed using a Python script, based on the orientation matrix method of Tauxe & Watson
562 (1994). For each magnetostratigraphic section the bootstrap reversal test (Tauxe et al., 1991) has
563 been carried out separately. In the TV and KA sections the normal and reverse polarities
564 directions are antipodal and the reversal test is positive (Figure 7h). On the contrary in the GH
565 section the normal and reverse polarities are not antipodal and the bootstrap reversal test is
566 negative, suggesting that data population could be partially affected by a recent magnetic
567 overprint that was not completely removed during stepwise demagnetization (Figure 7h). The
568 fold test was carried out for all the ChRM directions from the three stratigraphic sections (in total
569 373 direction) in order to have significant differences in the bedding attitudes. The mean
570 direction of the entire dataset is better grouped after tectonic correction (D = 7.5°; I = 40.0°, k =
571 6.3, $\alpha_{95\%}$ = 3.2°) rather than before (D = 308.8°, I = 74.2°, K = 4.4, $\alpha_{95\%}$ = 3.9) (Figure 7g). At
572 the same time, the bootstrap fold test (Tauxe et al., 1991) is positive showing that the degree of
573 unfolding to produce the maximum $\tau 1$ is between 86 and 106 % (Figure 7i). These results
574 demonstrate that the ChRM directions from the three stratigraphic sections were most likely
575 acquired before folding. Finally, it is worth to note that the mean ChRM direction obtained from
576 the three stratigraphic sections (D = 7.5°; I = 40.0°) is very similar to the one obtained from 14
577 sites from the same basin (D = 10.2°; I = 40.6°) with a positive reversal and fold tests (Mattei et
578 al., 2017). These data further support the primary origin of the ChRM in red beds of the URF as

579 also demonstrated by a recent paleomagnetic study in NE Iran (Mattei et al., 2019). On this basis
580 we are confident that our data allow determining correct polarities (latitude of the Virtual
581 Geomagnetic Poles, VGP) and hence to build up a reliable local magnetic polarity stratigraphy.
582
583 **4.3. Magnetostratigraphy**
584 The VGP latitudes from the new paleomagnetic data set define normal and reverse polarity
585 magnetozones (Figures 8e, 9e and 10e) and hence allow us to construct for each section a
586 magnetic polarity stratigraphy to be correlated with the Geomagnetic Polarity Time Scale
587 (GPTS) (Gradstein et al., 2012). In the following, we first correlate the KA section based on an
588 independent radiometric age, and then we correlate the underlying TV and the overlying GH
589 stratigraphic sections.
590
591 **4.3.1. KA stratigraphic section**
592 In the KA stratigraphic section 7 normal (N1-N7) and 8 reverse (R1-R8) polarity zones were
593 defined. A Zircon U-Pb age of 10.7 ± 0.4 Ma (Table 3) from an ash layer in the upper part of the
594 section at ~ 500 m suggests that the long-lasting normal polarity zone N1 should be correlated
595 with chron C5n1n. Consequently, the two short reverse polarity zones R1 and R2 and the longer
596 normal polarity zone N2 should belong to the same C5 chron. According to these correlations,
597 the polarity zones N3, N4, N5 as well as the reverse polarity zones R3, R4, R5 and R6 should
598 correspond to chron C5A. In the lower part of the section, the normal and reverse polarity zones
599 N6 and R7 can be correlated with chron C5AA, while the long lasting normal polarity (N7) and
600 the short reverse polarity zone at the base of the section can be correlated to chron C5AB. Based

601 on this correlation the most likely depositional age for the KA stratigraphic section will be
602 between ~ 13.6 to 10.3 Ma (Figure 9).
603
604 **4.3.2. TV stratigraphic section**
605 Patterns of VGP latitudes in section TV define 4 normal and 2 reverse polarity zones denoted as
606 N1-N4 and R1-R2, respectively. Stratigraphically, the TV section lies underneath the KA
607 stratigraphic section (Figure 2), thus we correlate the uppermost long normal polarity zone N1
608 and the reverse polarity zone R1 with chron C5AC. Consequently, the long normal polarity zone
609 N2 in the middle part of the section is correlated with chron C5AD and the short normal polarity
610 zone N3 with chron C5B. One reverse polarity zone in chron C5AD, one short normal as well as
611 a reverse polarity zone in the upper part of chron C5B in the GPTS are missing in our records.
612 Besides these three incompatibilities, which represent the time period between ca. 14.6 to 15.1
613 Ma, we successfully matched up each chron with the GPTS. We note that the missing chrons
614 come from the lower part of the section where the sedimentation rate is lower (~ 0.025 mm/yr)
615 (Figure 11) and the probability to miss a chron greater. The reverse polarity zone R2 in the
616 lowermost part of the section should correspond to chron C5B, while the long normal polarity
617 zone N4 at the base of the section should correlate with chron C5C. Accordingly, a depositional
618 age of ~ 16.5 to 13.7 Ma is proposed for the TV stratigraphic section (Figure 8).
619
620 **4.3.3. GH stratigraphic section**
621 Patterns of VGP latitudes in section GH define 10 normal and 9 reverse polarity zones, denoted
622 as N1-N10 and R1-R9, respectively. Stratigraphic sections KA and GH overlap, hence, in our
623 tentative correlation we associate the long-lasting, distinctive normal polarity zone N1 of section

KA with the normal zone N5 in the middle part of section GH. The uppermost normal polarity zones N1, N2 and N3 as well as the short reverse polarity zone R1 and long-lasting reverse polarity zones R2 and R3 at the top of the section can be correlated with chron C4. Consequently, the normal and reverse polarity zones N4 and R4 correlate with chron C4A. The long-lasting normal polarity zone N5 in the middle part of the section as well as the two short normal polarity zones N6 and N7 and two long reverse polarity zones R5 and R6 correspond to chron C5. Finally, the normal polarity zones N8, N9 and N10 and the reverse polarity zones R7, R8 and R9 in the lowermost part of the section should correlate with chron C5A. Based on this correlation the depositional age of section GH should range from ~13.2 to 7.6 Ma (Figure 10). Combined our data document a depositional age for the red beds in Tarom Basin from ~ 16.5 to at least 7.6 Ma. Importantly, this implies that these red clastics belong to the Upper Red Formation.

4.4. Sediment accumulations rates

The sediment accumulation rates for each stratigraphic section were calculated based on the magnetostratigraphic correlations and the stratigraphic thickness measured in the field (Figure 11). The oldest record (from ~ 16.5 Ma) is from the TV section where rates are relatively low (0.025 mm/yr) until ~ 14.6 Ma when an increase up to ~ 0.1 mm/yr occurs. From ~ 13.6 Ma the record includes both the GH and KA sections with similar rates of ~ 0.21 mm/yr at least until ~ 12.1 Ma. By ~ 12.1 Ma, sediment accumulation rates for the GH section increase up to ~ 0.29 mm/yr and remain higher than those in the KA section (at least until the top of the KA section at ~ 10.3 Ma). At the top the section, sediment accumulation rates decrease down to 0.15 mm/yr. Overall, the sediment accumulation rates from the intermontane Tarom Basin are slightly lower

than those recorded in the Miocene foreland basins of N Iran (0.3 to 2.2 and 0.3 to 0.5 mm/yr for the southern Alborz Mountains and the Great Pari Basin, respectively; Ballato et al., 2008, 2017) but they are still comparable with rates observed in tectonically active regions of the Alpine-Himalayan orogenic belt (e.g., Charreau et al., 2005; Huang et al., 2006; Zhu et al., 2008; Chang et al., 2012).

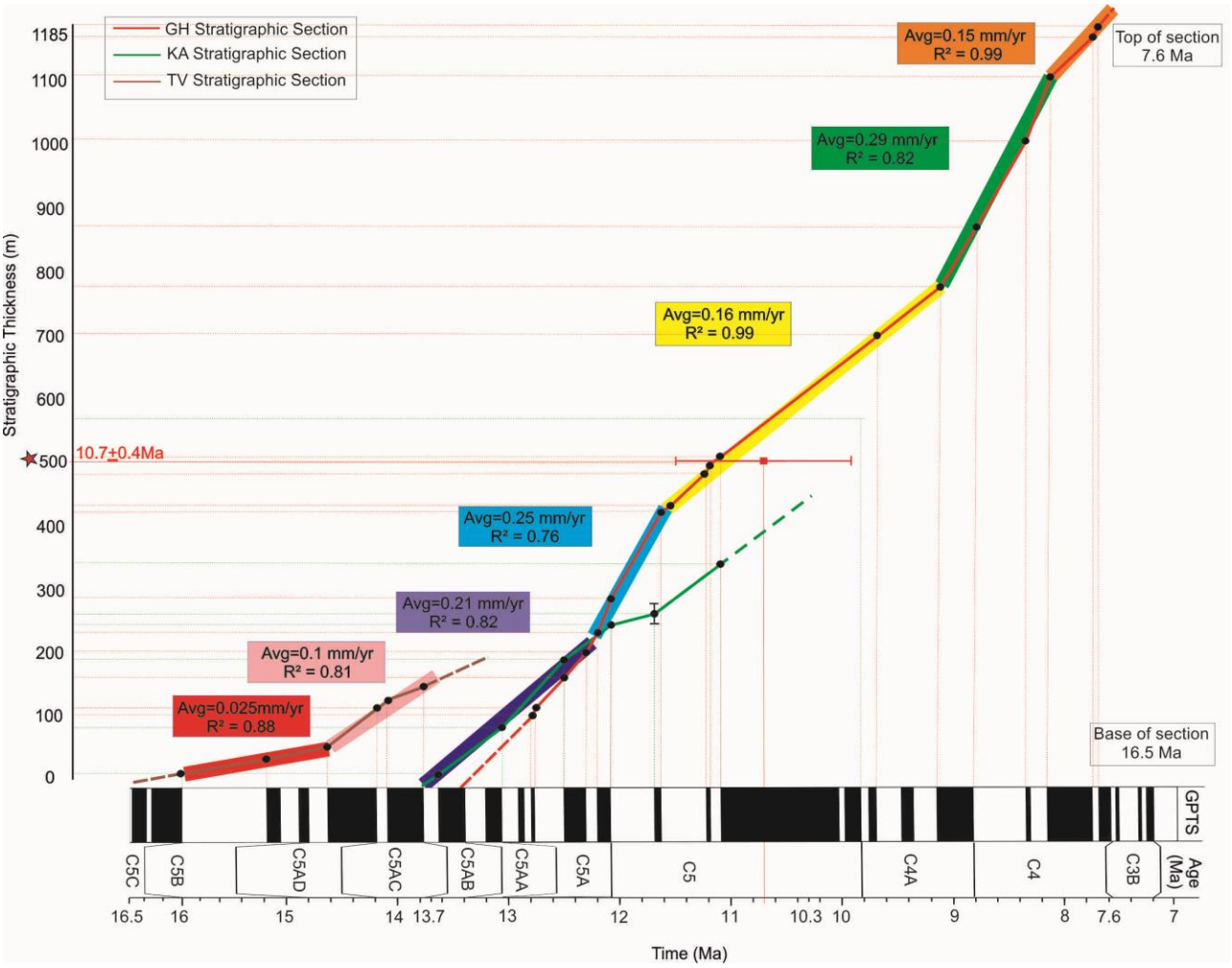

Figure 11. Long-term sediment accumulation rates for the Miocene synorogenic sediments of the three investigated stratigraphic sections. Rates have been obtained by using a linear best fit model (see correlation coefficient R^2) according to the different segments shown with the colourful boxe

658 **4.5. Sandstone petrography**

659 Petrographic analyses were performed on 6 thin sections collected along the KA and GH
660 stratigraphic sections according to the Gazzi-Dickinson method (Ingersoll, et al., 1984). Results
661 are plotted on QFL-c, QFL and Lm-Lv-Ls ternary diagrams (Figures 12a-c, respectively,
662 Dickinson et al., 1985; Garzanti, 2019). A detailed table can be found in the Appendix (Tables
663 A3.1 and A3.2). The KA sandstones are rather homogenous and mainly composed of volcanic
664 mafic clasts (Lvm, 50 and 58%) and plagioclase (Pl) grains (Figures 12a, 12c, 12d, 12g and 12h).
665 These are more abundant in the lower part of the section (30 vs 19%). A few lithic meta felsic
666 particles (Lmv; 6 to 9%) as well as a small amount (less than 5%) of quartz and heavy minerals
667 (epidote) are the other constituents observed in the KA samples. Finally, a minor amount (≤ 3%)
668 of lithic fragments such as lithic volcanic felsic (Lvf), lithic limestone (Lcc), lithic terrigenous
669 (Lp), lithic metasedimentary (Lms) and metabasalt lithic fragment (Lmb) were also observed.
670 Conversely, the GH sandstone samples contain a lower proportion of volcanic lithics, and a
671 higher proportion of low-grade metamorphic particles (Figures 12b, 12c, 12e, 12f and Table
672 A3.1).

673 The most abundant constituent of the framework components is represented by lithic
674 metasedimentary (Lms) clasts, which range upsection from 14 to 37% (Table 1). The second
675 most abundant constituents are lithic terrigenous (Lp; 8-25%). Other particles that are much
676 more abundant than in the KA samples are meta felsic (Lmv) and lithic limestone (Lcc) clasts (4
677 to 17% and 9 to 16%, respectively). Volcanic mafic clasts (Lvm) are less abundant than in the
678 KA samples and show a significant upsection decrease from 21 to 3%. Quartz (Figures 12e and
679 12i) and feldspar particles were also observed in GH sandstones (Figures 12d and 12h). Feldspar
680 grains are less abundant than in the KA samples, with plagioclase particles ranging from 3 to

10%, while the alkali feldspars display also a very small amount (1%). Instead, Quartz grains are more abundant (9 to 13%). A minor amount (≤ 3%) of other lithic fragments (Lvf, Lch, Lmf) and heavy minerals (such as epidote) were also observed.

Overall, the abundance of volcanic clasts in the KA samples indicates that the main sediment source along the southern margin of the basin must have been from the Eocene volcanics (Karaj Formation) of the Tarom range. It should also be noted that while the thin sections from the KA do not present any clasts of intrusive rocks, the unconformable conglomerates of supposed Pliocene contains abound clasts of granitoides, which are currently exposed along the southern slope of the range (Figure 2). This indicates post 7.6 Ma exposure of the granitoides of the Tarom range. Concerning the central sectors of the basin, the occurrence of metamorphic and sedimentary lithics, as well as the progressive decrease in volcanic grains suggests that the central sectors of the basin (GH samples) where mostly sourced from the northern basin margin (Alborz Mountains). This agrees with paleocurrent directions obtained in different sectors of the GH stratigraphic section (Figure 10).

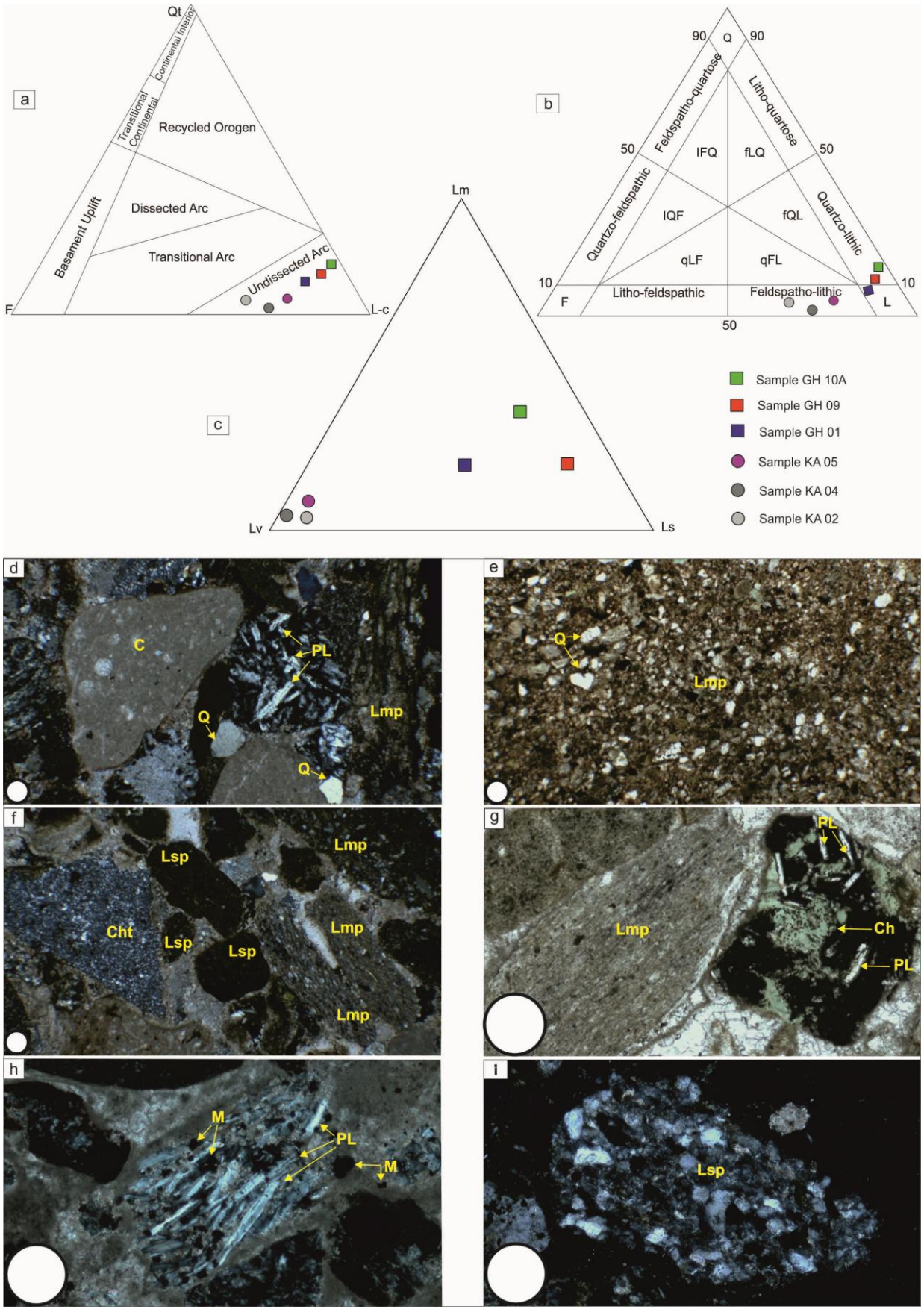
a
Qt
Continental Interior
Transitional Continental
Recycled Orogen
Basament Uplift
Dissected Arc
Transitional Arc
Undissected Arc
F
L-c
b
Q
90
90
Feldspatho-quartose
Litho-quartose
50
50
IFQ
fLQ
Quartzo-feldspathic
Quartzo-lithic
IQF
fQL
qLF
qFL
10
10
F
Litho-feldspathic
Feldspatho-lithic
L
50
c
Lm
Lv
Ls
Sample GH 10A
Sample GH 09
Sample GH 01
Sample KA 05
Sample KA 04
Sample KA 02
d
C
PL
Lmp
Q
Q
e
Q
Lmp
f
Lsp
Lmp
Cht
Lsp
Lsp
Lmp
Lmp
g
PL
Lmp
Ch
PL
h
M
PL
M
i
Lsp

695

Figure 12. QFL triangular diagrams with tectonic zones defined by (a) Dickinson, (1985) and (b) Garzanti, (2019). Q represents total quartz grains (Qm = monocrystalline and Qp = polycrystalline), F represents total feldspar grains (P = plagioclase and K-feldspars), L total lithic clasts and L-c: total lithic clasts excluding carbonates. (c) Lm-Lv-Ls ternary plot for the Tarom Basin (Lm = metamorphic; Lv = volcanic; Ls = sedimentary). (D to I) Representative photomicrographs of sandstone samples. (d) Sample GH-16-05 (stratigraphic position of ~ 410 m) showing a large calcareous grain (c), a volcanic mafic grain with plagioclases (PL), a slate fragment with rough cleavage (Lmp) and quartz grains. (e) Sample GH-16-04 (at ~ 370 m) with metamorphic clasts and quartz (Q) grains in a terrigenous-carbonatic matrix. (f) Sample GH-16-05 (at ~ 410 m) with chert (Cht), pelitic lithic (Lsp) and metamorphic fragments (Lmp). (g) Sample GH-16-10B (~ 990) showing a volcanic mafic grain (Lvm) with Pl altered in green Chlorite (Ch), and Lmp. (h) Sample KA-16-05 (~ 450) displaying a volcanic mafic grain with Pl and magnetite (M) crystals. (I) Sample GH-16-01 (~ 75 m) showing a sandy siltstone lithic fragment with detrital micas (Lsp). Note that all photos are under cross polarized light except figure f. Small and large white circles show scales of 4 and 10 microns, respectively.

5. Discussion and Conclusions

Based on our new age determinations and the reconstruction of the depositional systems and sediment dispersal patterns we propose a four-stage evolutionary model for the Tarom Basin for the last ~38-36 Ma (Figure 13a-d) and we discuss the main implications of our findings for the lateral (orogen perpendicular) evolution of the IP, including the mechanisms that led to the growth of its northern margin (Figure 14).

5.1. ~38-36-16.5 Ma: topographic growth of the southern margin, formation of angular unconformities and development of external drainage conditions

The geometrical relationships among the strata of the Karaj Formation exposed along the southern sectors of the Tarom Basin suggest that minor folding must have occurred during the

latest stages of Eocene arc volcanism around 38-36 Ma (Figures 3b and 6). This could represent the earliest event of Late Eocene-Early Oligocene collisional deformation recorded across the entire Arabia-Eurasia collision zone from the Zagros to the Caucasus, Talesh, Alborz and Koph Dagh mountains (Vincent et al., 2007; Morley et al., 2009; Ballato et al., 2011, 2015; Mouthereau et al., 2012; Rezaeian et al., 2012; Roberts et al., 2014; Tadayon et al., 2018). Furthermore, our Middle-Late Miocene age of the overlying red beds indicates that the topographic growth of the Tarom range prevented the Late Oligocene-Early Miocene marine transgression that led to the deposition of the shallow-marine sediments of the Qom Formation (Figure 14a; e.g., Reuter et al., 2009). Therefore, between 38-36 Ma and ~ 16.5 Ma (initiation of red beds sedimentation) the Tarom Basin must have experienced external drainage conditions. This implies that the eroded sediments were delivered directly to the Caspian Sea and hence a connection between the Tarom Basin and Caspian Sea must have been established after the end of arc volcanism (Figure 14a). Sometime during this ~ 20-My-long period both basin margins experienced tilting that led to the development of an angular unconformity between the Karaj Formation and the overlying red beds (Figure 3). Prior to that, the Alborz Mountains represented a topographic barrier between central Iran and the Caspian Sea as suggested by the lack of Eocene volcanics along the northern slope of the Alborz (Figure 14a; Guest et al., 2006a).

5.2. ~16.5 to < 7.6 Ma: intermontane basin development and internal drainage conditions

Sedimentation of continental red beds in the Tarom Basin started at ~ 16.5 Ma and lasted at least until 7.6 Ma. This indicates that these sediments are stratigraphically equivalent to the Upper Red Formation (e.g., Ballato et al., 2008, 2017). During that time interval sedimentation occurred in an intermontane basin developed most likely as flexural response to tectonic loading from the adjacent uplifting mountain ranges (Alborz Mountains to the N and Tarom range to the S;

Figures 13b and 14a). Basin development was associated with a sharp increase in sediment accumulation rates (one order of magnitude, from 0.025 to 0.21 mm/yr) along the TV section at ~14.6 Ma (Figure 11). Furthermore, the occurrence of lacustrine and playa lake deposits in the basin depocenter implies the development of internally drained conditions associated with the topographic growth of the Alborz Mountains, which must have disconnected the former drainage system from the Caspian Sea. Such a topographic growth was triggered by widespread regional deformation related to a more advanced stage of the Arabia-Eurasia collision (e.g., Ballato et al., 2011; Mouthereau et al., 2012) in agreement with available low-temperature thermochronology data in NW Iran (Guest et al., 2006b; Rezaeian et al., 2012; Ballato et al., 2013, 2015; Madanipour et al., 2013, 2017). This is further corroborated by the presence of growth strata along the north margin of the basin indicating syndepositional contractional deformation (Figures 2, 3e and 13b-d).

Our sediment provenance data provide additional information on to the evolution of the sediment source area. The southern side of the basin received sediments from the growing Tarom range. There, exhumation has been limited to less than 3-4 km as documented by available 41-32-My-old apatite fission track ages that may still record magmatic cooling (Rezaeian et al., 2012). This is also shown by the sandstone petrography data from the KA section, that have a rather constant composition dominated by volcanic lithics and feldspars (feldspatho-lithic arenite; QFL plot; Figure 12b), as expected for undissected arc regions (QtFL-c ternary diagram; Figure 12a). Instead, the central part of the basin received a greater amount of sediments from the Alborz Mountains as documented by the higher proportion of metamorphic lithics and quartz grains (quartzo-lithic arenite; Figure 12b). Although these sample plot also in the undissected arc (Figure 12a), the upsection increase in metamorphic grains and the relative decrease in volcanic

lithics suggests erosional unroofing with the progressive exposure of the metamorphic basement. This agrees with a fully reset Miocene apatite fission track age (Rezaeian et al., 2012) indicating that exhumation along the Alborz Mountains was greater than in the Tarom range.

5.3. <7.6 Ma to Pliocene? drainage reintegration, basin uplift, deformation and erosion

Sometime after ~7.6 Ma, the Tarom Basin was reintegrated into an external drainage system and a new fluvial connection with the Caspian Sea developed. One possible cause could be fluvial headward erosion triggered by the km-scale, base level drop of the Caspian Sea between ~ 5.5 and 3 Ma (Forte & Cowgill, 2013;). Alternatively, basin capture may have occurred through overspill from the Tarom Basin into the Caspian Sea. In any case, after 4 Ma, the Tarom Basin must have been integrated into the drainage system of the Qezwl-Owzan as documented by overflow processes from the adjacent and more elevated Mianeh Basin of the Iranian Plateau that led to the development of ~1-km-deep Amardos gorge (Figure 1; Heidarzadeh et al., 2017). The establishment of an external drainage system appears to coincide with intrabasinal deformation, basin uplift and erosion, as recorded by several post 7.6 Ma anticline-syncline pairs, in the central sectors of the basin (Figures 2 and 3h). This is well visible in the central sectors of the study area (GH section) where the occurrence of subvertical to overturned red beds suggests the development of a north verging anticline most likely associated with a detachment horizon within gypsum layers at the base of the red beds.

5.4. Pliocene? to Present: alternating episodes of basin aggradation, incisions and excavation

Following intrabasinal deformation, the Tarom Basin experienced at least one major episode of (supposed) Pliocene conglomerate deposition (Stocklin, 1969; Figure 3a) as well as three main

793 phases of basin aggradation and incision, as documented by distinct levels of Quaternary terrace
794 conglomerates (Figures 2, 3a and 13d). These unconformable deposits suggest the occurrence of
795 alternating phases of limited (or absent) and efficient fluvial connectivity with the Caspian Sea.
796 A similar configuration has been described in the intermontane basins of arid to semiarid
797 climatic regions like those forming the Eastern Cordillera and the broken foreland of NW
798 Argentina. There, the landscape response to Quaternary climate changes is thought to be the
799 main driver of short-term cycles (10^5 years) of basin filling and excavation, while tectonics plays
800 a major role in controlling the long-term filling history (10^6 years; Strecker et al., 2009; Streit et
801 al., 2015; Schildgen et al., 2016; Tofelde et al., 2017; Ballato et al., 2019; Pingel et al., 2019).
802 Here, the lack of chronological constraints does not allow unravelling the role of different
803 forcing mechanisms. In any case, it should be noted that, the supposed Pliocene conglomerates
804 are slightly folded into a broad syncline suggesting a possible interplay between intrabasinal
805 deformation and sedimentary loading/unloading cycles, which can hinder/promote intrabasinal
806 deformation (Ballato et al., 2019). For example, these conglomerates are in unconformity onto
807 folded Miocene red beds, therefore, their deformation must have occurred after their deposition
808 either during or after their removal through fluvial erosion (i.e., during sedimentary unloading).
809 Finally, it should be noted that a similar long-term, tectono-stratigraphic history has been
810 proposed for the intermontane Taleghan-Alamut basin of the central-western Alborz Mountains
811 (Guest et al., 2007). There, the deposition of Middle-Late Miocene red beds was followed by
812 Late Miocene-Pliocene intrabasinal deformation, Pliocene aggradation with conglomerate
813 deposition and Quaternary fluvial incision. This common evolution suggests that the orogen may
814 have responded along strike in a similar way to (either tectonic or climatic) forcing mechanisms
815 (Ballato et al., 2015).
816

817

818

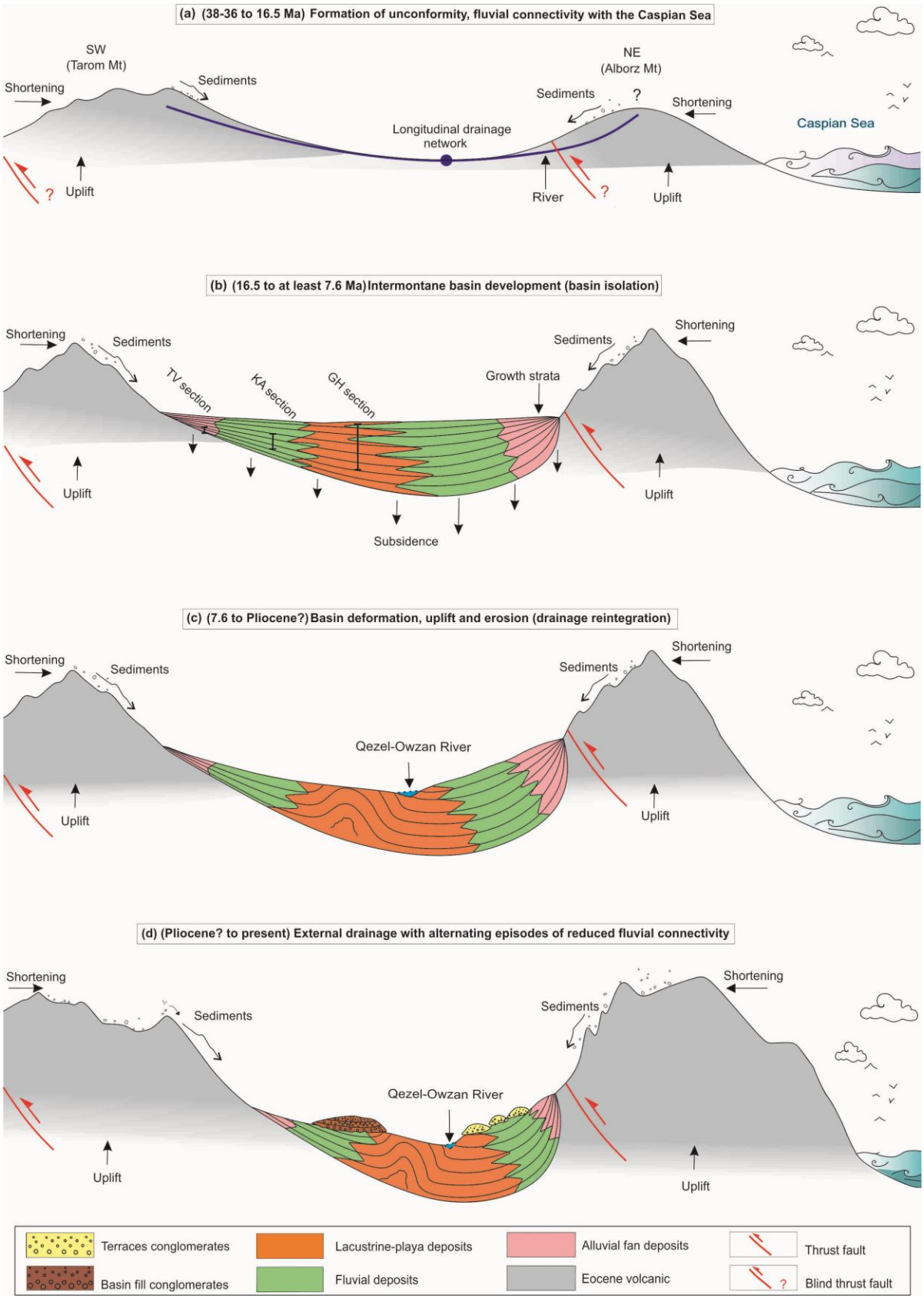
(a) (38-36 to 16.5 Ma) Formation of unconformity, fluvial connectivity with the Caspian Sea
SW
(Tarom Mt)
Shortening
Sediments
Longitudinal drainage
network
NE
(Alborz Mt)
Sediments
?
Shortening
Caspian Sea
?
Uplift
River
?
Uplift
(b) (16.5 to at least 7.6 Ma) Intermontane basin development (basin isolation)
Shortening
Sediments
TV section
KA section
GH section
Growth strata
Sediments
Shortening
Uplift
Uplift
Subsidence
(c) (7.6 to Pliocene?) Basin deformation, uplift and erosion (drainage reintegration)
Shortening
Sediments
Qezel-Owzan River
Sediments
Shortening
Uplift
Uplift
(d) (Pliocene? to present) External drainage with alternating episodes of reduced fluvial connectivity
Shortening
Sediments
Qezel-Owzan River
Sediments
Shortening
Uplift
Uplift
Terraces conglomerates
Basin fill conglomerates
Lacustrine-playa deposits
Fluvial deposits
Alluvial fan deposits
Eocene volcanic
Thrust fault
Blind thrust fault

819

Figure 13. Schematic diagram showing the Late Cenozoic evolution of the Tarom Basin (a) ~38-36-16.5 Ma, uplift and tilting, formation of angular unconformities, and development of an external drainage system flowing into the Caspian Sea. (b) ~ 16.5-7.6 Ma, basin isolation and internal drainage conditions, development of an intermountain basin, uplift of the basin-bounding mountain ranges (Tarom and Alborz ranges). The red bars show the location of three measured stratigraphic sections (c) ~7.6 Ma-Pliocene? drainage reintegration with renewed fluvial connectivity with the Caspian Sea, intrabasinal deformation, basin uplift and erosion. (d) Pliocene? to present, cycles of incision and aggradation, folding of basin fill conglomerates.

5.5. Implications on plateau building processes

Our multidisciplinary dataset provides new insights into the lateral (orogen perpendicular) development of the Iranian Plateau and the vertical growth of its northern margin (Tarom range). The hinterland of IP recorded foreland sedimentation starting from ~ 16.5 Ma, shortly after the Late Oligocene-Early Miocene marine transgression that led to the deposition of the Qom Formation (Ballato et al., 2017; Figure 14a). This implies that plateau uplift must be younger than ~ 16.5 Ma. Flexural subsidence was triggered by mountain building processes along the plate suture zone as documented by early Miocene low-temperature thermochronology data from the Sanandaj-Sirjan Zone (Francois et al., 2014; Barber et al., 2018). Foreland basin initiation in the plateau interior coincided with the development of the endorheic Tarom Basin and hence with Middle Miocene topographic growth along the northern sectors of the Arabia-Eurasia collision zone (Ballato et al., 2011, 2013, 2015; Rezaeian et al., 2012). Such a configuration indicates that the retroforeland basin of the Arabia-Eurasia collision zone was partitioned into a broken foreland, like in the North American Cordillera and the South American Andes (e.g., Jordan & Allmendinger 1986; Strecker et al., 2012). The retroforeland was compartmentalized after ~ 11 Ma (Ballato et al., 2017) through the growth of few, orogen parallel, mountain ranges in the plateau interior, which appear to have a regular wavelength of 40-50 km (Figures 14b and

14c). This led to the development of few internally drained intermontane basins and eventually of a typical low-relief plateau morphology (Sobel et al., 2003; Garcia Castellanos et al., 2007), that is still preserved in the sectors of the plateau that are internally drained (Figure 1).

Interestingly, while uplift in the broken foreland of the Andes occurred through the reactivation of steep basement faults (Sierra Pampeanas; e.g., Jordan & Allmendinger 1986) or listric reverse faults (Santa Barbara System; e.g., Kley & Monaldi, 2002) that extend up to at least ~ 25 km of depth (Alvarado et al., 2007; Richardson et al., 2012), the IP presents a more complex pattern of deformation and a shallow seismicity (maximum depth of 20 km, with the majority of the hypocenters around 10 km; Maggi et al., 2002). Although a clear structural model for the IP is currently missing, there are no evidences for a dominant vergence toward the upper plate with a lower crust décollement rooted into the plate boundary as documented in the Altiplano and Puna plateaus (e.g, Horton et al., 2018). A possible reason could be that Iran represents a mobile orogenic belt (e.g., Faccenna et al., 2010) where different microplates were accreted and sutured from the early Triassic (Zanchi et al., 2009; Wilmesen et al., 2009). This has produced some peculiar characteristics such as: 1) the occurrence of orogenic sutures and several crustal scales anisotropies that were repeatedly reactivated under extensional (Late Jurassic and Eocene; e.g., Brunet et al., 2003; Zanchi et al., 2006; Verdel et al., 2011) and compressional (Late Cretaceous to Paleocene and latest Eocene to Oligocene; Guest et al., 2006; Zanchi et al., 2006; Yassaghi & Madanipour, 2008; Rezaeian et al., 2012; Madanipour et al., 2017) regimes before widespread Miocene collisional deformation (e.g., Ballato et al., 2011, 2013; Mouthereau et al., 2012); 2) the presence of a composite stratigraphy (Figure 14b) with few episodes of accelerated subsidence along different depocenters that led to the deposition of several km-thick clastic (the Late Triassic, Shemshak Formation; e.g., Wilmsen et al., 2009; the Miocene, Upper Red Formation,

e.g., Ballato et al 2017) and volcaniclastic (the Eocene Karaj Formation; Verdel et al., 2011) sedimentary sequences; 3) the occurrence of a warm lithosphere associated with Eocene magmatism that continued in several sectors of the IP until the present (e.g., Chiu et al., 2013; Rabiee et al., 2020).

During the growth of the IP margin, the Tarom Basin recorded continues syntectonic sedimentation at least until ~ 7.6 Ma with the accumulation of more than ~1.2 km of red clastics. Low-temperature thermochronology data document an acceleration in fault-related exhumation along both margins of the Tarom Basin starting from 12-10 Ma (Rezaeian et al., 2012; Madanipour et al., 2017), in agreement with our sediment accumulation rates. At the same time, our sandstone petrography data suggest that the Alborz Mountains experienced a greater magnitude of exhumation than the Tarom range. This implies that topographic growth in the Tarom range was associated with limited erosional exhumation, as also documented by the occurrence of subdued topography onlapped by basin-fill units in the plateau interior (Heidarzadeh et al., 2017). This suggests that most of the Miocene convergence within the upper plate must have been absorbed via crustal shortening and thickening in the western Alborz Mountains and in the plateau interior rather than along its northern margin. This agrees with a recent seismological study indicating a Moho depth of at least 45 km in the plateau interior that tapers northward to ~ 35 km underneath the northern plateau margin and the Tarom Basin, and increase up to 40-45 km beneath the western Alborz (Figure 14c; Motaghi et al., 2018). Importantly, the occurrence of a ~ 35 km-deep Moho beneath the Tarom range, which is more elevated than the thickened plateau interior, suggests that crustal shortening and thickening cannot be responsible for the topographic growth of the plateau margin. Therefore, surface uplift along the Tarom, must have been triggered by deep-seated, mantle driven processes (e.g.,

Hatzfeld & Molnar, 2010) rather than crustal/lithospheric shortening and thickening (e.g., Sobel et al., 2003). One possible cause could be the removal of a thickened lithospheric mantle sometimes between 12 and 10 Ma, when deformation processes appears to have accelerated across Northern Iran (Hatzfeld & Molnar, 2010; Francois et al., 2014), and widespread uplift seems to have occurred in the plateau interior (Figure 14b; Ballato et al., 2017). This agrees with the occurrence of a thin lithospheric mantle across most of the upper plate (Rahmani et al., 2019, and references therein), from the suture zone to the Caspian Basin. In any case, although paleoaltimetric data are not yet available and therefore there are not constraints on the vertical growth of the plateau, our reconstruction shows that: 1) the lateral (orogen perpendicular) expansion of the plateau must have occurred over the last 11 Ma, and 2) by 11 Ma the IP must have reached a lateral size similar to present-day one.

Finally, the reconstruction of the basin fills history of the Tarom Basin and our field observations do not indicate the presence of elevations like those attained by the intermontane basins of the plateau interior. This shows that the Tarom Basin was never incorporated into the IP during its phases of internal drainage or limited connectivity with the Caspian Sea. Such a conclusion agrees with a shallow Moho beneath the Tarom Basin (Figure 14c) and corroborates the idea that topographic ponding

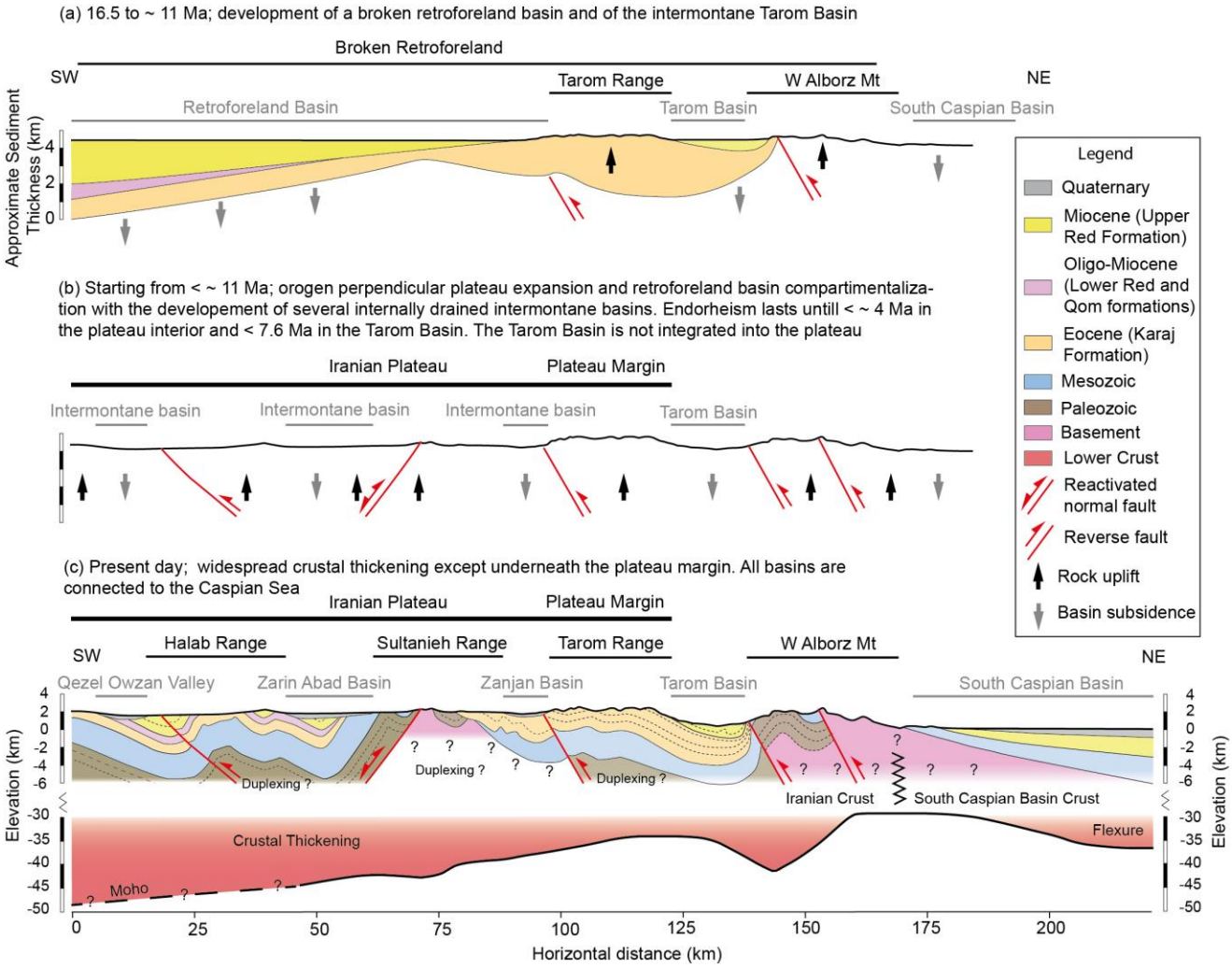

Figure 14. (a and b) Schematic reconstruction of the Late Cenozoic, broken, retroforeland basin of the Arabia Eurasia collision zone during the orogen perpendicular expansion of the Iranian Plateau (see text for details). (c) Geologic cross section (see figure 1 for location) based on Stocklin & Eftekharnezhad, (1969), Davies (1977) and our field observations, and Moho depth (solid line) from Motaghi et al., (2018). The dashed line is extrapolated from the trend in crustal thickness across the IP shown in Rahmani et al., (2019).

5.6. Conclusions

Our work represents the first detailed study in the Tarom Basin, an intermontane basin at the transition between the Iranian Plateau and the Alborz Mountains. Combined, our data show that the regional, Eocene arc volcanism in this area ended at ~ 38-36 Ma in association with the onset

of low-magnitude compressional deformation. This was followed by a prolonged phase of erosion with development of angular unconformities. By ~16.5 Ma, the topographic growth on the northern side of the basin (western Alborz Mountains) must have disconnected the Tarom Basin from the Caspian Sea, leading to the formation of an internally drained intermontane basin. Our new ages document that the synorogenic deposits of the Tarom range are stratigraphically equivalent to the Miocene Upper Red Formation. The accommodation space available for sedimentation was most likely controlled by lithospheric flexural in response to tectonic loading of the adjacent mountain ranges. Internal drainage conditions lasted at least until ~7.6 Ma, when basin incision and excavation occurred in association with intrabasinal deformation. Subsequently the occurrence of supposed Pliocene conglomerates and at least three Quaternary terrace conglomerates indicate multiple phases of aggradation and incision. This cyclic behaviour occurred during alternating episodes of reduced and renewed fluvial connectivity with the Caspian Sea. The lack of a detailed chronology, however, does not allow understanding the forcing mechanisms for these cycles. In any case, the elevation of the Tarom Basin during endorheic conditions did not reach those one of the plateau interiors, therefore, the basin was not morphologically integrated into the IP. Furthermore, our reconstruction indicates that the plateau was built on the broken retroforeland of the Arabia-Eurasia collision zone. Specifically, a retroforeland basin developed starting from ~16.5 Ma during tectonic loading and topographic building along the plate suture zone. This coincided with topographic growth along the northern sectors of the collision zone and the development of the intermontane Tarom Basin. Starting from ~11 Ma, intraforeland uplift led to the compartmentalization of the basin with the growth of several mountain ranges over a typical wavelength ~40-50 km and intervening endorheic intermontane basins. During this process the plateau reached a lateral size (orogen perpendicular)

like the present one. The northern margin of the IP (Tarom Range) experienced limited erosional exhumation and crustal thickening, suggesting that the vertical growth of the plateau must have been triggered by deep-seated processes (delamination of thickened lithospheric mantle?) rather than crustal shortening and thickening, possibly by 12-10 Ma when upper plate deformation accelerated.

Acknowledgments

This study is part of the PhD thesis of MP at the University of Roma Tre (PhD program Cycle XXXII) and was supported by the PhD School of Roma Tre, the MIUR (Ministry of Education University and Research; Grant Rita Levi Montalcini to PB), the DFG (German Science Foundation; grants DFG BA 4420/2-1 and BA 4420/2-2 to PB) and the DAAD (German Academy Research Service, grant to GH). The authors declare no financial or other conflicts of interest. Software and analyzed data of paleomgantic samples used to produce the results in this work are available at https://data.mendeley.com/drafts/n5z4h9dy6x/DOI:10.17632/n5z4h9dy6x.2.

The authors would like to thank Masoud Biralvand and Mahmood Fallah for helping with the logistic during the field work.

Appendix

In the following we provide a detailed description of the analytical procedures for each methodology used in this thesis. The raw data can be found in form of tables and figures.

A1. Zircon U-Pb-dating

A2. Zircon U-Pb-dating

A3. Sandstone petrography

A1. Zircon U-Pb-dating

Mineral separation was performed according to standard techniques (crushing, sieving, water table, magnetic separation and heavy liquids as needed) at the Institute of Earth and Environmental Science of the University of Potsdam. Zircons grains where sent to the the Geochronology Laboratory in the Department of Earth and Space Sciences, University of California Los Angeles for the sample preparation and the laboratory measurements. Epoxy grain mounts of hand-selected zircons were gently ground to expose grain interiors and were given final polish with 1 µm diamond. After ultrasonic cleaning, grains were surveyed for internal compositional zonations and/or inclusions via cathode luminescence (CL) imaging. Mounts were then coated with ~100Å of Au. U-Pb ages were determined based on U, Pb, and Th isotopic spot measurements using the UCLA CAMECA ims 1270 ionprobe following the analytical procedure explained in Schmitt et al. (2003). Each analytical run collected data for ten cycles, and age calculations were performed by means of ISOPLOT (Ludwig, 2003). The final ages listed in Table 3 of chapter 2 represent the weighted mean at the 95% confidence level for a given number of aliquots ranging from two to seven (Figure A1.1; Mahon, 1996).

References

Ludwig, K.R. (2003). User's Manual for Isoplot/Ex, A geochronological toolkit for Microsoft Excel Berkeley Geochronology Center Special Publication, v. 4, Berkeley Geochronology Center, 2455 Ridge Road, Berkeley, CA 94709, USA.

Schmitt, A.K., Grove, M., Harrison, T.M., Lovera, O.M., Hulen, J. & Waters, M. (2003). The Geysers–Cobb Mountain magma system, California (Part 1): U-Pb zircon ages of volcanic rocks,

conditions of zircon crystallization and magma residence times. Geochimica et Cosmochimica Acta, 67, 3423–3442.

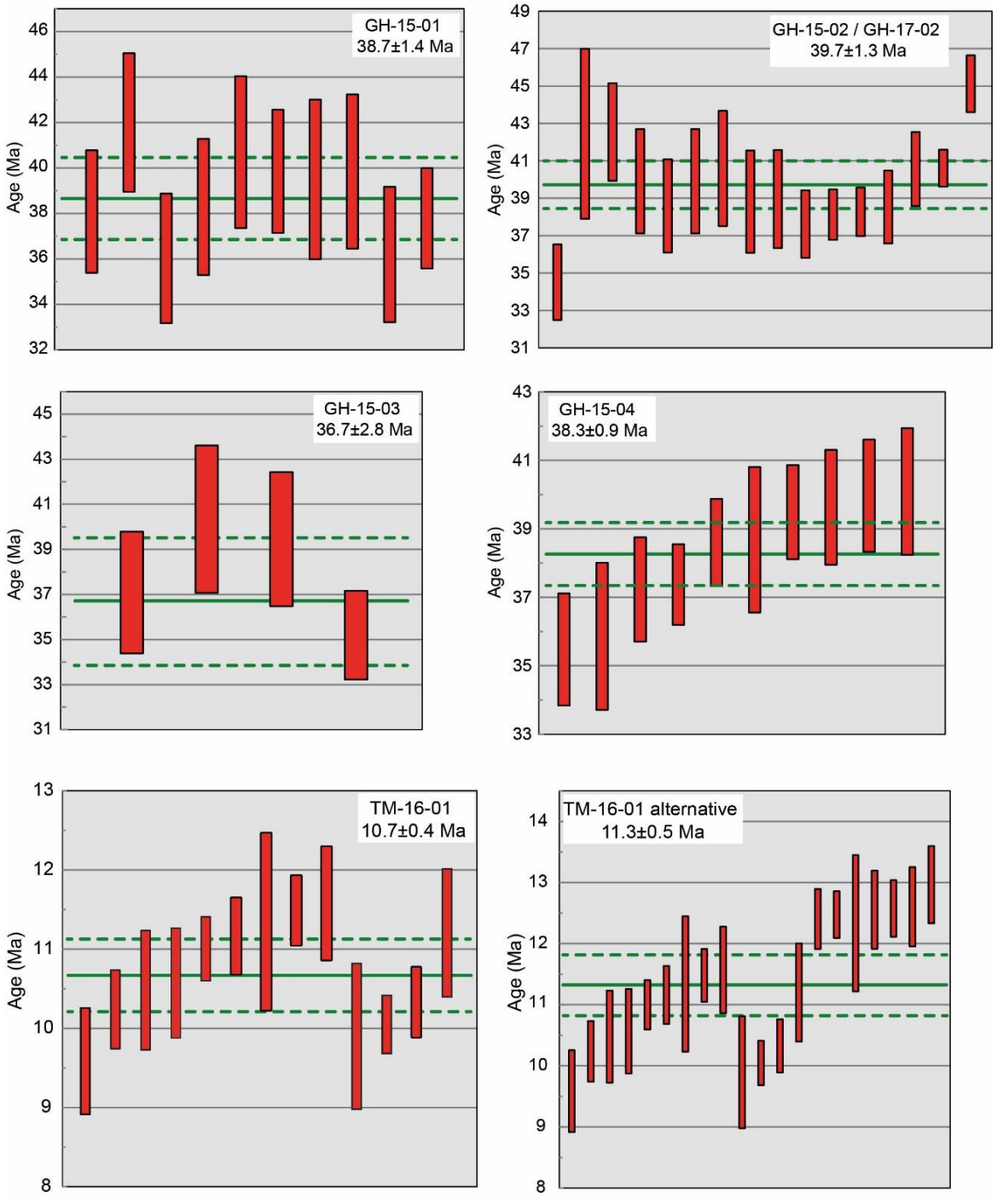

Figure A1: Weighted averages for the analyzed samples shown with a green lines and associated error (in two sigmas) in a dashed green line. The red boxes display the raw data of selected grains (2 sigma error). For sample TM-16-01, two possible solutions are shown (see section 4.1; geochronology for details).

A2. Zircon U-Pb-dating

A total of 536 oriented samples were collected from the three investigated stratigraphic section (TV, GH and KA section) for a combined stratigraphic thickness of 1185 m. The mean sampling interval is typically ~ 3m with at least two cores at each site. In case of poor outcrop conditions or in sectors composed mostly of coarse-grained sediments the sampling intervals was as large as ~ 5-6 m. All the samples were cored with a portable gasoline-powered drill. The orientations of the cores were measured by using a magnetic compass to determine both azimuth of core axis (declination) and dip of the core axis (inclination) and also corrected for ~ 5º E present day declination using magnetic field calculators (www.ngdc.noaa).

Magnetic measurements were then performed using a 2-G Enterprises superconducting rock magnetometer equipped with DC-SQUID coils within a magnetically shielded room at the Alpine Laboratory of Paleomagnetism (ALP) at Peveragno (Turin) and at the INGV Laboratory of Paleomagnetism (Rome, Italy) shielded room in Rome, both in Italy. After measuring the Normal Remanent Magnetization (NRM), samples were subjected to stepwise (up to 15 steps) thermal demagnetization, using heating routine increments (150°C up to a temperature of 480°C and 30–50°C increments above 480°C) until the signal decreased below the instrumental detection limit or random changes of the paleomagnetic directions occurred. A set of sister specimens were chosen for AF demagnetization. Stepwise alternating field (AF) demagnetizations were done using a three-axis demagnetizer with a maximum field of up to 100/120 mT, coupled with a 2G–DCSQUID magnetometer. Data processing was conducted by

means of Rema soft program and led to the isolating the stable polarity directions of the characteristic remanent magnetization (ChRM) by using the principal component analysis (Kirschvink, 1980), data statistical analysis by means of Fisher statistics (Fisher, 1953), and finally the calculation of the Virtual Geomagnetic Pole (VGP) from the ChRM vectors.

References

Fisher, R.A. (1953). Dispersion on a sphere, Proceedings of the Royal Society of London, Series A, 217, 295–305.

Kirschvink, J.L. (1980). The least-squares line and plane and the analysis of palaeomagnetic data, Geophysical Journal of the Royal Astronomical Society, 62, 699-718.

A3. Sandstone petrography

Six sandstone samples collected from the KA and GH sections in the Tarom basin were analyzed under a polarized microscope in transmitted light (Table A3.1). In each sample, 400 points were counted by using the Gazzi-Dickinson method (Ingersoll et al. 1984) the results of the modal analysis are plotted in the ternary diagrams of Garzanti (2019) and Dickinson (1985) in order to identify the local tectonic setting and the sediment provenance area (Table A3.1 and Table A3.2).

Table A3.1

Sandstone composition of the KA and GH stratigraphic studied sections in the Tarom Basin

	QFL; Garzanti (2019)			QtFL-c; Dickinson (1985)		
Sample Number	Q	F	L	Qt	F	L-c
KA-16-02	5	31	64	4	32	64
KA-16-04	1	27	72	1	27	72
KA-16-05	5	20	75	5	20	75
GH-16-01	9	10	81	13	12	75
GH-16-09	11	5	83	15	7	78

GH-16-10A	13	4	83	15	4	81

Note. (1) QFL by Garzanti (2019); (Q) Total quartz grains (Qm = monocrystalline + Qp = polycrystalline), (F): Total feldspar grains (P = plagioclase + K-feldspars), (L) Total lithic fragments. (2) QtFL- by Dickinson (1985); (Qt) Total quartzose grains (Qm + Qp), (F) Total feldspar grains (P + K), L-c: Total lithic fragments (excluding carbonates).

Table A3.2

Lm-Lv-Ls ternary plot for the Tarom basin

Sample Number	Lm	Lv	Ls
KA-16-02	5	89	6
KA-16-04	6	93	1
KA-16-05	7	88	5
GH-16-01	20	39	41
GH-16-09	20	13	67
GH-16-10A	36	17	47

Note. (Lm = metamorphic; Lv = volcanic; Ls = sedimentary)

References

Dickinson, W.R. (1985). Interpreting provenance relations from detrital modes of sandstones. In: Zuffa, G.G. (Ed.), Provenance of arenites. Reidel, Dordrecht, NATO ASI Series, 148, 333–361.

Garzanti, E.D. (2019). Petrographic classifiation of sand and sandstone. Earth-Science Reviews, 192, 545–563.

Ingersoll, R.V., Bullaed, T.F., Ford, R.L., Grimm, J.P., Pickle, J.D. & Sares, S.W. (1984). The effect of grain size on detrital modes: a test of the Gazzi–Dickinson point-counting method. Journal of Sedimentary Petrology, 54, 103 –116.

References

Abimbola, D.A. (2016). A Re-evaluation of the Depositional Environments and Sedimentary Facies of Middle Miocene Paralic Deposits (Agbada Formation), Ewan and Oloye Fields, Northwestern Niger Delta. Journal of Marine Science: Research & Development.

Agard, P., Omrani, J., Jolivvet, L., Whitechurch, H., Vrielynck, B., Spakman, W., Monie, P., Meyer, B., & Wortel, R. (2011). Zagros orogeny: A subduction-dominated process. Geol. Mag, 148 (5–6), 689–691.

Allmendinger, R.W., Jordan, T.E., Kay, S.M., & Isacks, B.L. (1997). The evolution of the Altiplano-Puna Plateau of the central Andes. Journal of Annual Review of Earth and Planetary Sciences, 25, 139–174.

Alvarado, P., Beck, S., & Zandt, G. (2007). Crustal structure of the south-central Andes Cordillera and backarc region from regional waveform modelling. Journal of Geophys. J. Int., 170, 858–875, doi: 10.1111/ j.1365-246X.2007.03452.x.

Alonso, B., E Field, M., V Gardner, J., & Maldoando, A. (1990). Sedimentary evolution of the Pliocene and Pleistocene Ebro margin. northeastern Spain. Marine Geology, 95, 313-331.

Amini, B. (1969). Geological map of Tarom. Geological Survey of Iran, Tehran, scale 1:100,000

Maggi, A., Jackson, J.A., McKenzie, D. & Priestley, K. (2000). Earth-quake focal depths, effective elastic thickness, and the strengthof the continental lithosphere. Geology, 28. 459–498

Ballato, P., Brune, S., & Strecker, M.R. (2019). Sedimentary loading–unloading cycles and faulting in intermontane basins: Insights from numerical modelling and field observations in the NW Argentine Andes. Earth and Planetary Science Letters, 506, 388-396.

Ballato, P., Cifelli, F., Heidarzadeh, G.H., Ghassemi, M.R., Wicert, A.D., Hassanzadeh, J., Dupont–nivet, G., Balling, P., Sudo, M., Zeiliger, G., Schmit, A.K., Mattei, M., & Strecker, M.R. (2017). Tectono-sedimentary evolution of the northern Iranian Plateau: insights from middle-late Miocene foreland-basin deposits. Basin Research, 29, 1–30.

Ballato, P., Landgraf, A., Fox, M., Stockli, D., Schildgen, T.F., Ghassemi, M.R., Kirby, E., & Strecker, M.R. (2015). The growth of a mountain belt forced by base-level fall: tectonics and surface processes during the evolution of the Alborz Mountains, N Iran. Earth Planet. Sci. Lett, 425, 204–218.

Ballato, P., Nowaczy, N.R., Landgraf, A., Strecker, M.R., Friedrich, A., & Tabaei, S.H. (2008). Tectonic control on sedimentary facies pattern and sediment accumulation rates in the Miocene foreland basin of the southern Alborz Mountains, northern Iran. Tectonics, 27, TC6001.

Ballato, P., Stockli, D.F., Ghassemi, M.R., Landgraf F, A., Strecker, M.R., Hassanzadeh, J., Friedrich, A., & Tabatabei, S.H. (2013). Accommodation of transpressional strain in the Arabia-Eurasia collision zone: new constraints from (UTh)/He thermochronology in the Alborz Mountains, N Iran. Tectonics, 32, 1–18.

Ballato, P., Uba, C.E., Landgraf, A., Strecker, M.R., Sudo, M., Stockl, D.F., Friedrich, & A., Tabatabei, S. H. (2011). Arabia-Eurasia continental collision: Insights from late Tertiary foreland-basin evolution in the Alborz Mountains, northern Iran. Geological Society of America Bulletin, 123, 106–131.

Barber, D.E., Stockli, D.F., Horton, B.K., & Koshnaw, R.I. (2018). Cenozoic Exhumation and Foreland Basin Evolution of the Zagros Orogen During the Arabia-Eurasia Collision, Western Iran. Tectonics, 37, 4396–4420. https://doi.org/10.1029/2018TC005328.

Berberain, M., & Walker, R. (2010). The Rudbār Mw 7.3 earthquake of 1990 June 20; seismotectonics, coseismic and geomorphic displacements, and historic earthquakes of the western 'High-Alborz', Iran. Geophysical Journal International, 182, 1577–1602.

Blair, T.C. (1999). Sedimentology of the debris-flow–dominated Warm Spring Canyon alluvial fan, Death Valley, California. Sedimentology, 46, 941–965.

Boothroyd, J.C., & Ashletey, G.M. (1975). Processes, bar morphology, and sedimentary structures on braided outwash fans, Northeastern Gulf of Alaska. The Society of Economic Paleontologists and Mineralogist (SEPM); Glaciofluvial and Glaciolacustrine Sedimentation (SP23).

Borradaile, G.J., & Henry, B. (1997). Tectonic applications of magnetic susceptibility and its anisotropy. Earth Sci Rev, 42, 49–93.

Borradaile, G. J. (1988). Magnetic susceptibility, petrofabrics and strain. Tectonophysics, 156, 1-20.

Borradaile, G. J. (2001). Magnetic fabrics and petrofabrics: Their orientation distribution and anisotropies. J. Struct. Geol, 23, 1581–1596.

Brunet, M., Korotaev, M.V., Ershov, A.V., & Nikishin, A.M. (2003). The South Caspian Basin: a review of its evolution from subsidence modelling. Sedimentary Geology, 156, 119-148.

Carroll, A.R., Graham, S.A., & Smith, M.E. (2010). Tectonic and Stratigraph. Evolution of Nonmarine Basins of China. Basin Research, 22, 17 - 32.

Castellanos, D.G. (2007). The role of climate during high plateau formation Insights from numerical experiments. Earth and Planetary Science Letters, 257, 372–390.

Charreauh, J., Chen, Y., Gilder, S., Dominguez, S., Avouac, J.PH. Sen, S., Sun, D., Li, Y., & Wang, W.M. (2005). Magnetostratigraphy and rock magnetism of the Neogene Kuitun He section (northwest China): Implications for Late Cenozoic uplift of the Tianshan mountains. Earth and Planetary Science Letters, 230, 177–192.

Chiu, H.-Y., Chung, S.-L., Zarrinkoub, M.H., Mohammadi, S.S., Khatib,M.M., & Iizuka, Y. (2013). Zircon U–Pb age constraints from Iran on the magmatic evolution related to Neotethyan subduction and Zagros orogeny. Lithos, 162–163, 70–87.

Cifelli, F., Ballato, P., Alimohammadian, H., Sabouri, J., & Mattei, M. (2015). Tectonic magnetic lineation and oroclinal bending of the Alborz range: Implications on the Iran-Southern Caspian geodynamics. Tectonic, 234, 116-132.

Davies, R.G. (1977). Geological map of Bandar e Pahlavi quadrangle. Geological Survey of Iran, Tehran, scale 1:250,000.

Davies, D., Suppe, J., & Dahlen, F.A. (1983). Mechanics of fold-and-thrust belts and accretionary wedges. J. Geophys. Res, 88, 1153–72.

Davoudzadeh, M., Lammerer, B., & Weber-Diefenbach, K. (1997). Paleogeography, Stratigraphy, and Tectonics of the Tertiary of Iran. Neues Jahrbuch für Geologie und Paläontologie – Abhandlungen, 205, 33-67.

Dewey, J.F., & Burke, K. (1974). Hot spots and continental break-up: implications for collisional orogeny. Geology, 2, 57–60.

Dewey, J.F. (1988). Extensional collapse of orogens. Tectonics, 7, 1123–1139.

Dickinson, W.R. (1985). Interpreting provenance relations from detrital modes of sandstones. In: Zuffa, G.G. (Ed.), Provenance of arenites. Reidel, Dordrecht, NATO ASI Series, 148, 333–361.

Djamour, Y., Vernant, P.H., Bayer, R., Nankali, H.R., Ritz, J.F., Hinderer, J., Hatam, Y., Luck, B., & Moigne, N.L. (2010). GPS and gravity constraints on continental deformation in the Alborz Mountain range, Iran. Geophysical Journal International, 183, 1287-1301.

Dupont-Nivet, G., & Krijgsman, W. (2012). Magnetostratigraphic methods and applications, in Busby, C., Azor, A. (eds.), Recent Advances in Tectonics of Sedimentary Basins, Wiley-Blackwell, p 80-94.

Ejiuba, C., Heubeck, C., & Hulka, C. (2005). Facies analysis and basin architecture of the Neogene Subandean synorogenic wedge, southern Bolivia. Sedimentary Geology, 180, 91–123.

Engdahl, E., Jackson, J., Myers, S., Bergman, E., & Priestley, K. (2006). Relocation and assessment of seismicity in the Iran region. Geophys. J. Int, 167, 761–788.

England, P.H., & Mvkenzie, D. (1982). A thin viscous sheet model for continental deformation. Geophysical Journal of the Royal Astronomical Society, l70, 295–32.

Francois, T., Agard, P., Bernet, M., Meyer, B., Chung, S.L., Zarrinkoub, M.H., Burov, E. & Moni_E, P. (2014). Cenozoic exhumation of the internal Zagros: first constraints from low-temperature thermochronology and implications for the build-up of the Iranian plateau. Lithos, 206–207, 100–112.

Faccenna, C., Becker, T.W., Jolivet, L. & Keskin, M. (2013). Mantle convection in the Middle East: reconciling Afar upwelling, Arabia indentation and Aegean trench rollback. Earth Planet. Sci. Lett., 373, 254–269.

François, T., Burov, E., Agard, P., & Meyer, B. (2014). Buildup of a dynamically supported orogenic plateau: Numerical modeling of the Zagros/Central Iran case study, Geochem. Geophys. Geosyst., 15, 2632–2654, doi:10.1002/2013GC005223.

Forte, A.M., & Cowhill, E. (2013). Late Cenozoic base-level variations of the Caspian Sea: a review of its history and proposed driving mechanisms. Palaeogeogr. Palaeo-climatol. Palaeoecol, 386, 392–407.

Francois, T., Burov, E., Agard, P., & Meyer, B. (2014). Buildup of a dynamically supported orogenic plateau: Numerical modeling of the Zagros/Central Iran case study; Geochem. Geophys. Geosyst, 15, 2632–2654.

Garzanti, E.D. (2019). Petrographic classifiation of sand and sandstone. Earth-Science Reviews, 192, 545–563.

Chang, H., An, ZH., Liu, W., Qiang, X., Song, Y., & Ao, H. (2012). Magnetostratigraphic and paleoenvironmental records for a Late Cenozoic sedimentary sequence drilled from Lop Nor in the eastern Tarim Basin, Global and Planetary Change, 80–81, 113–122.

Ghinass, M., D'oriano, F., Benvenuti, M., Fedi, M., & Awramik., S. (2015). Lacustrine Facies in Response to Millennial-Century-Scale Climate Changes (Lake Hayk, Northern Ethiopia), Journal of Sedimentary Research, 85, 381–398.

Chakraborty, T., & Soumendar, S. (2005). Evidence of lacustrine sedimentation in the Upper Permian Bijori Formation, Satpura Gondwana basin, Palaeogeographic and tectonic implications, Journal of Earth System Science, 114, 303–323.

Ghibaudo, G.U. (1992). Subaqueous sediment gravity flow deposits: practical criteria for their field description and classification. Sedimentology (IAS), 39, 423-454.

Gradstein, F.M., Ogg, J.G., Schmitz, M., & Ogg, G. (2012). The Geologic Time Scale 2012. Elsevier, Cambridge University Press, Cambridge.

Guest, B., Axen, G.J., Lam, P.S., & Hassanzadeh, J. (2006a). Late Cenozoic shortening in the west central Alborz Mountains, northern Iran, by combined conjugate strike-slip and thin-skinned deformation. Geosphere, 2, 35–52.

1241 Guest, B., Horton, B.K., Axen, G.J., Hassanzadeh, J., & Mcintosh, W.C. (2007). Middle to late
1242 Cenozoic basin evolution in the western Alborz Mountains: Implications for the onset of
1243 collisional deformation in northern Iran. Tectonics, 26, TC6011.
1244
1245 Guest, B., Stockli, D. F., Grove, M., Axen, G. J., Lam, P. S., & Hassanzadeh, J. (2006b).
1246 Thermal histories from the central Alborz Mountains, northern Iran: Implications for the spatial
1247 and temporal distribution of deformation in northern Iran. Geological Society of America
1248 Bulletin, 118, 1507-1521.
1249
1250 Hassanzadeh, J., Stockli, D. F., Horton, B. K., Axen, G. J., Stockl, L. D., & Grove, M. (2008). U-
1251 Pb zircon geochronology of late Neoproterozoic- Early Cambrian granitoids in Iran: Implications
1252 for paleogeography, magmatism, and exhumation history of Iranian. 778 basement.
1253 Tectonophysics, 451, 71–96.
1254
1255 Hatzfeld, D., & Molnar, P. (2010). Comparisons of the kinematics and deep structures of the
1256 Zagros and Himalaya and of the Iranian and Tibetan plateaus and geodynamic implications, Rev.
1257 Geophys, 48, 2.
1258
1259 Heidarzadeh, G.H., Ballato, P., Hassanzadeh, J., Ghassemi, M.R., & Strecker, M.R. (2017). Lake
1260 Overspill and onset of fluvial incision in the Iranian Plateau: insights from the Mianeh Basin;
1261 Planetary Science Letters 469, 135-147.
1262

Hein, F.J. (1982). Depositional mechanisms of deep-sea coarse clastic sediments, Cap Enrage Formation, Quebec. Canadian Journal Earth Science, 19, 267–287.

Hermannas, R.L., & Strecker, M.R. (1999). Structural and lithological controls on large Quaternary rock avalanches (sturzstroms) in arid northwestern Argentina. Geological Society of America Bulletin, 111, 934-948.

Hilley, G.E, Strecker, M.R., & Ramos, V.A. (2004). Growth and erosion of fold-and-thrust belts with an application to the Aconcagua fold-and-thrust belt, Argentina. J. Geophys. Res, 109, B1.

Hilley, G.E., & Strecker, M.R. (2004). Steady state erosion of critical Coulomb wedges with applications to Taiwan and the Himalaya. J. Geophys. Res, 109, B1.

Horton, B.K., Hassanzadeh, J., Stockli, D.F., Axen, G.J., Gillis, R.J., Guest, B., Amini, A., Fakhari, M.D., Zamanzadeh, S.M., & Grove, M. (2008). Detrital zircon provenance of Neoproterozoic to Cenozoic deposits in Iran: Implications for chronostratigraphy and collisional tectonics: Tectonophysics, 451, 97–122.

Horton, B.K. (2018). Tectonic regimes of the Central and Southern Andes: responses to variations in plate coupling during subduction. Tectonics, 37 (2), 402–429.

Horton, K.B., & Schmitt, J.G. (1996). Sedimentology of a lacustrine fan-delta system, Miocene Horse Camp Formation, Nevada, USA. Sedimentology, 43, 133–155.

Horton, B. K. (2012). Cenozoic evolution of Hinterland Basins in the Andes and Tibet. In C. Busby, & A. Azor (Eds.), *Tectonics of Sedimentary Basins: Recent advances* (pp. 427–444). New York, NY: John Wiley & Sons, Ltd.

Hrouda, F. (1982). Magnetic anisotropy of rocks and its application in geology and geophysics. Suveys in Geophysics, 5, 37–82.

Huang, B., Piper, J.D.A., Peng, SH., Liu, T., LI, ZH., Wang, Q., & Zhu, R. (2006). Magnetostratigraphic study of the Kuche Depression, Tarim Basin, and Cenozoic uplift of the Tian Shan Range, Western China, Earth and Planetary Science Letters, 251, 346–364.

Ilgar, A., & Nemec, W. (2005). Early Miocene lacustrine deposits and sequence stratigraphy of the Ermenek Basin, Central Taurides, Turkey, Sedimentary Geology, 173, 233-275.

Ingersoll, R.V., Bullaed, T.F., Ford, R.L., Grimm, J.P., Pickle, J.D., & Sares, S.W. (1984). the effect of grain size on detrital modes: a test of the Gazzi–Dickinson point-counting method. Journal of Sedimentary Petrology, 54, 103 –116.

Isacks, B.L. (1988). Uplift of the central Andean Plateau and bending of the Bolivian Orocline, J. Geophys. Res 93, 3211–3231.

Jimenez-Munt, I., Fernandez, M., Saura, E., Verges, J., & Garcia-Castellanos, D. (2012). 3-D lithospheric structure and regional/residual Bouger anomalies in the Arabia-Eurasia collision (Iran). Geophys. J. Int 190, 1311–1324.

Jordan, T.E. & Allmendinger, R.W. (1986). The Sierras Pampeanas of Argentina: a modern analogue of Rocky Mountain foreland deformation. Am. J. Sci., 286, 737–764.

Keighiley, D. (2008). A lacustrine shoreface succession in the Albert Formation, Moncton Basin, New Brunswick, Bulletin of Canadian Petroleum Geology, 56, 235-258.

Kley, J., & Monaldi, C.R. (2002). Tectonic inversion in the Santa Barbara system of the central Andean foreland thrust belt, northwestern Argentina: Tectonics, v. 21, p. 1–18, 1061.

Kodama, K.P. (2012). Paleomagnetism of Sedimentary Rocks: Process and Interpretation Science, p 184.

Koshnaw, R.I., & Stockli, D.F. (2018). Timing of the Arabia-Eurasia continental collision-Evidence from detrital zircon U-Pb geochronology of the Red Bed Series strata of the northwest Zagros hinterland, Kurdistan region of Iraq. Geology, 47, 47-50.

Kraus, M.J. (1999). Paleosols in clastic sedimentary rocks: their geologic applications. Earth Science Reviews, 47, 41-70.

Lamb, S., Hoke, L., Kennan, L., & Dewey, J. (1997). Cenozoic Evolution of the Central Andes in Bolivia and Northern Chile, ed. JP Burg, M Ford, 121, 237–64.

Langereis, C.G, Krijgsman, W., Muttoni, G., & Menningning, M. (2010). Magnetostratigraphy; concepts, definitions, and applications. Newsletter on Stratigraphy, 43/3, 207–233.

Larrasoana, J.C., Pueyo, E.L., & Pares, J.M. (2004). An integrated AMS, structural, palaeo- and rock-magnetic study of Eocene marine marls from the Jaca-Pamplona basin (Pyrenees, N Spain); new insights into the timing of magnetic fabric acquisition in weakly deformed mudrocks. Geological Society, London, Special Publications, 238 (1), 127.

Lowenstein, T.K., & Hardie, L.A. (1985). Criteria for the recognition of salt-pan evaporites. Sedimentology, 32, 627–644.

Madanippur, S., Ehlres, T., Yassaghi, A., Rezaeian, M., Enkelmann, E., & Bahroudi, A. (2013). Synchronous deformation on orogenic plateau margins: insights from the Arabia-Eurasia collision. Tectonophysics, 608, 440–451.

Madanippur, S., Ehlres, T.A., Yassaghi, A., & Enkelmann, E. (2017). Accelerated middle Miocene exhumation of the Talesh Mountains constrained by U-Th/He thermochronometry: Evidence for the Arabia-Eurasia collision in the NW Iranian Plateau. Tectonics, 36, 1538-1561.

Madanippur, S., Yassaghi, A., Todd Ehllers, T.A., & Enkelmann, E. (2018). Tectonostratigraphy, structural, geometry and kinematics of the NW Iranian Plateau margin: Insight from the Talesh Mountains, Iran. American Journal of Science, 318, 208-245.

Maizels, J. (1989). Sedimentology, paleoflow dynamics and flood history of jokulhlaup deposits; paleohydrology of Holocene sediment sequences in southern Iceland sandur deposits. Journal of Sedimentary Research, 59, 204-223.

Mattei, M., Cifelli, F., Muttoni, G., & Rashid, H. (2015). Post-Cimmerian (Jurassic–Cenozoic) paleogeography and vertical axis tectonic rotations of Central Iran and the Alborz Mountains. J. Asian Earth Sci, 102, 92–101.

Mattei, M., Cifelli, F., Alimohammaadian, H., Rashid, H., Winkert, A., & Sagnotti, L. (2017). Oroclinal bending in the Alborz Mountains (Northern Iran): New constraints on the age of South Caspian subduction and extrusion tectonics, Gondwana Research, 42, 13-28.

Mattei, M., Visconti, L. A., Cifelli, F., Nozaem, R., Winkert, A., & Sagnotti, L. (2019). Clockwise paleomagnetic rotations in north-eastern Iran: Major implications on recent geodynamic evolution of outer sectors of the Arabia-Eurasia collision zone, Gondwana Research, 71, 194-209.

Mattei, M., Cifelli, F., Alimohammaadian, H., & Rashid, H. (2020). The role of active strike-slip faults and opposite vertical axis rotations in accommodating Eurasia-Arabia shortening in Central Iran. Tectonophysics, 774, 228-243.

Mcfadden, P.L., & Mcelhinny, M.W. (1990). Classification of the reversal test in palaeomagnetism. Geophys. J. Int, 103, 725–729.

Meyer, B., Tappnnnier, P., Bourjot, L., Me´tiver, F., Gaudemer, Y., Peltzer, G., Guo, S., & Chen, Z. (1998). Crustal thickening in Gansu-Qinghai, lithospheric mantle subduction, and oblique, strike-slip controlled growth of the Tibet Plateau. Geophys. J. Int, 135, 1– 47.

Miall, A.D. (1978). Lithofacies types and vertical profile models in braided river deposits. Fluvial Sedimentology: Canadian Society Petrology Geology Memoir, 5, 597–604.

Miall, A.D. (1985). Architectural-Element Analysis: A New Method of Facies Analysis Applied to Fluvial Deposits. Earth-Science Reviews, 22, 261-308.

Miall, A.D. (1996). The Geology of Fluvial Deposits. Springer Verlag, Berlin XVI, 582 pp.

Miall, A.D. (1997). A review of the braided river depositional environment. Earth Science Review, 13, 1–62.

Monlar, P., England, PH., & Martiod, J. (1993). Mantle dynamics, uplift of the Tibetan Plateau, and the Indian Monsoon. Reviews of Geophysics, 31, 357-396.

Motaghi, K., Ghods, A., Sobouti, F., Shabanian, E., Mahmoudabadi, M., & Priestly, K. (2018). Lithospheric seismic structure of the West Alborz – Talesh ranges, Iran. Geophysical Journal International, 215, 1766-1780.

Morley, C., Kongwung, B., Julapour, A.A., Abdolghafourian, A., Hajian, M., Waples, D., Warren, J., Otterdoom, H., Srisuriyon, K., & Kazemi, H. (2009). Structural development of the major Late Cenozoic basin and transpressional belt in Central Iran: the Central Basin in the Qom-Saveh area. Geosphere, 5, 325–362.

Mouthereau, F., Lacombe, O., & Verges, J. (2012). Building the Zagros collisional orogen: timing, strain distribution and the dynamics of Arabia/Eurasia plate convergence. Tectonophysics, 532-535, 27-60.

Mouthereau, F., Lacombe, O., & Verges, J. (2012). Building the Zagros collisional orogen: timing, strain distribution and the dynamics of Arabia/Eurasia plate convergence. Tectonophysics, 532-535, 27-60.

Nabatian, GH. Ghaderi, M., Neubauer, F., Honaemand, M., Liu, X., Dong, Y., Jjang, S.H.Y., Quadt, A.V., & Bernroider, M. (2014). Petrogenesis of Tarom high-potassic granitoids in the Alborz-Azarbaijan belt, Iran: Geochemical, U-Pb zircon and Sr–Nd–Pb isotopic constraints. Lithos, 184-187, 324-345.

Omrani, H., Moazzen, M., Oberhansli, R., Tsujimori, T., Bousquet, R., & Moayyed, M. (2013). Metamorphic history of glaucophane-paragonite-zoisite eclogites from the Shanderman area, northern Iran. Journal of Metamorphic Geology, 31, 791-812.

Paknia, M., Ballato, P., & Mattei, M. (2019). An integrated paleomagnetic, rock magnetic, anisotropy of magnetic susceptibility, stratigraphic and structural study of Miocene synorogenic red beds from NW Iran: Insight into the geologic evolution of the intermontane Tarom Basin at the linkage between the western Alborz Mountains and the northern margin of the Iranian Plateau.

PhD thesis; chapter III, Department of Science, Unievrsity of Roma Tre, Ciclo Del Corso Di Dottorato XXXII.

Pares, J.M. (2004). How deformed are weakly deformed mudrocks? Insights from magnetic magnetic anisotropy. In: Martin-Hernandez, F., Lüneburg, C., Aubourg, C., Jackson, M. (Eds.), Magnetic Fabrics: Methods and Applications. Geological Society, London, Special Publication, 238, 191–203.

Pingel, H., Alonso, R.N., Altenberger, U., Cottle J., & Strecker, M.R. (2019). Miocene to Quaternary basin evolution at the southeastern Andean Plateau (Puna) margin ca. 24°S lat, Northwestern Argentina. Basin Research, 32, 808-826.

Pingel, H., Schildgen, T., & Strecker, M.R. (2019). Hella Wittmann, Pliocene–Pleistocene orographic control on denudation in northwest Argentina. Geology, 47, 359-362.

Pirouzouz, M., Avouzc, J-P., Hassanzadeh, J., Kirschvink, J.L., & Bahroudi, A. (2017). Early Neogene foreland of the Zagros, implications for the initial closure of the Neo-Tethys and kinematics of crustal shortening. Earth and Planetary Science Letters, 477, 168–182.

Puy-Aquiza, M.J., Mirand-Aviles, R., Garcia-Barragan, J.C., Loza-Aguirre, I., Li, Y., & Anazanor, G. (2017). Facies analysis, stratigraphic architecture and depositional environments of the Guanajuato conglomerate in the Sierra de Guanajuato, Mexico. Boletín de la Sociedad Geológica Mexicana, 69, 385-408.

R. Merrill, R., Mcfadden, P., & Mcelhinny, M. (1996). The Magnetic Field of the Earth: Paleomagnetism, the Core, and the Deep Mantle. International geophysics series ISSN 0074-6142; Academic Press, San Diego, p 531.

Rabiee, A., Rossetti, F., Asahara, Y., Azizi, H., Glodny, J., Lucci, F., Lustrino, M., Nozaem, R. (2020). Long-lived, Eocene-Miocene stationary magmatism in NW Iran along a transform plate boundary, NW Iran, Gondwana Research.

Rahmani, M., Motaghi, K., Ghods, A., Sobouti, F., Talebian, M., Ai, Y., & Chen, L. (2019). Deep velocity image of the north Zagros collision zone (Iran) from regional and teleseismic tomography. Geophys. J. Int. 219, 1729–1740.

Reiners, P.W., & Brandon, M.T. (2006). Using thermochronology to understand orogenic erosion. Annu. Rev. Earth Planet. Sci, 34, 419–66.

Reuter, M., Piller, W. E., Harzhauser, M., Mandic, O., Berning, B., & Rogl, F. (2009). The Oligo-/Miocene Qom Formation (Iran): Evidence for an early Burdigalian restriction of the Tethyan Seaway and closure of its Iranian gateways. International Journal of Earth Sciences, 98, 627–650.

Rezaeian, M., Carter, A., Hovius, N., & Allen, M.B. (2012). Cenozoic exhumation history of the Alborz Mountains, Iran: New cconstraints from low-temperature chronometry. Tectonics, 31, TC2004.

Richardson, T., Gilbert, H., Anderson, M., & Ridgway, K.D. (2012). Seismicity within the actively deforming eastern Sierras Pampeanas, Argentina. Geophys. J. Int. 188, 408e420.

Ridgway, K.D., & Decelles, P.G. (1993). Stream-dominated alluvial fan and lacustrine depositional systems in Cenozoic strike-slip basins, Denali fault system, Yukon Territory, Canada. Sedimentology, l40, 645-666.

Rieben, H. (1955). The geology of the Tehran plain. American Journal of Science 253, 617–639.

Robert, A.M.M., Letouzey, J., Kavoosi, M.A., Sherkati, S.H., Muller, C., (2014). Structural evolution of the Kopeh Dagh fold-and-thrust belt (NE Iran) and interactions with the South Caspian Sea Basin and Amu Darya Basin. Marine and Petroleum Geology, Elsevier, 57, 68-87.

Robion, P., Grelaud, S., & Frizon de lamotte, D. (2007). Pre-folding magnetic fabrics in fold and-thrust belts: Why the apparent internal deformation of the sedimentary rocks from the Minervois basin (NE-Pyrenees, France) is so high compared to the Potwar basin (SW-Himalaya, Pakistan)? Sediment. Geol, 196, 181–200.

Royden, L. (1996). Coupling and decoupling of crust and mantle in convergent orogens: Implications for strain partitioning in the crust, J. Geophys. Res, 101, 17, 679–17, 705.

Royde, L.H., Burchfiel, B. C., King, R.W., Wang, E., Chen, Z., Shen, F., & Liu, Y. (1997). Surface deformation and lower crustal flow in Eastern Tibet. Science, 276 (5313), 788–790.

R.X., Potts, R., Pan, Y.X., Lu, L.Q., Yao, H.T., Deng, C.L., & Qin, H.F. (2008). Paleomagnetism of the Yuanmou Basin near the southeastern margin of the Tibetan Plateau and its constraints on late Neogene sedimentation and tectonic rotation, Earth and Planetary Science Letters, 272, 97–104.

Saint-Bezar, B., Hebert, R.L., Aubourg, C., Robion, P., Swenen, R. Frizon de, & Lamotte, D. (2002). Magnetic fabric and petrographic investigations of hematite-bearing sandstones within ramp-related folds: examples from the South Atlas Front (Morocco). J. Struct. Geol, 24, 1507–1520.

Schildgen, T., RobinsonI, R.A.J., Savi, S., Phillips, W.M., Sperncer, J.Q.G., Bookhangen, B., Scherler, D., Tofelde, S., Alonso, R.N., Kunik, P.W., Binnie, S.A., & Strecker, M.R. (2016). Landscape response to late Pleistocene climate change in NW Ar-gentina: sediment flux modulated by basin geometry and connectivity. J. Geo-phys. Res, 121, 392–414.

Siks, B.C., & Horton, B.K. (2011). Growth and fragmentation of the Andean foreland basin during eastward advance of fold-thrust deformation, Puna plateau and Eastern Cordillera, northern Argentina. Tectonic, 30.

Sobel, E.R., & Strecker, M.R. (2003). Uplift, exhumation and precipitation: Tectonic and climatic control of late Cenozoic landscape evolution in the northern Sierras Pampeanas, Argentina. Basin Research, 15, 431–451.

Sobel, E.R., Hilley, G.E., & Strecker, M.R. (2003). Formation of internally drained contractional basins by aridity-limited bedrock incision. J. Geophys. Res. Solid Earth, 108, JB001883.

Soto, R., Larrasoana, J.C., Arlegui, L.E., Beamud, E., Olivaurcia, B., & Simon, J.L. (2009). Reliability of magnetic fabric of weakly deformed mudrocks as a palaeostress indicator in compressive settings. J. Struct. Geol, 31, 512–522.

Stanistreet, I.G., & Mccarthy, T.S. (1993). The Okavango Fan and the classification of subaerial fan systems. Sedimentary Geology, 85, 115–133.

Stocklin, J., & Eftekharnezhad, J. (1969). Geological map of Zanjan quadrangle. Geological Survey of Iran, Tehran scale 1:250,000.

Strecker, M.R., Alonso, R., Bookhagen, B., Carrpapa, B., Coutand, I., Hain, M.P., Hilley, G.E., Mortimer, E., Schoenbohm, L., & Sobel, E.R. (2009). Does the topographic distribution of the central Andean Puna Plateau result from climatic or geodynamic processes. Geology, 37, 643–646.

Strecker, M. R., Hilley, G. E., Bookhagen, B., & Sobel, E. R. (2012). Structural, geomorphic, and depositional characteristics of contiguous and broken foreland basins: Examples from the eastern flanks of the central Andes in Bolivia and NW Argentina, in Tectonics of Sedimentary Basins: Recent Advances, edited by C. Busby and A. Azor, pp. 508–521, John Wiley, Chichester, UK. doi: 10.1002/9781444347166.ch25

Strecker, M.R., Alonso, R.N., Bookhagen, B., Carrpapa, B., Hilley, G.E., Sobel, E.R., & Ttruth, M.H. (2007). Tectonics and Climate of the Southern Central Andes. Annu. Rev. Earth Planet, 35, 747-787.

Streit, R.L., Burbank, D.W., Strecker, M.R., Alonso, R.N., Cottle, J.M., & Kulander-Clark, A.R.C. (2015). Controls on intermontane basin filling, isolation and incision on the margin of the Puna plateau, NW Argentina (~23°S). Basin Research, 29, 131–155.

Tadayon, M., Rosseti, F., Zattin, M., Calzolari, G., Nozaem, R., Salvini, F., Cladio, F., & Khoabakhshi, P. (2018). The long-term evolution of the Doruneh Fault region (Central Iran): A key to understanding the spatio-temporal tectonic evolution in the hinterland of the Zagros convergence zone. Geological journal, 54, 1454-1479.

Tarling, D. H., & Hrouda, F. (1993). The Magnetic Anisotropy of Rocks. London: Chapman & Hall, 217 p.

Tha, H.V, Wysocka, A., Pha, P.D., Cuong, N.Q., & Ziolkowski, P. (2015). Lithofacies and depositional environments of the Paleogene/Neogene sediments in the Hoanh Bo Basin (Quang Ninh province, NE Vietnam). Geology, Geophysics & Environment, 41, 353–369.

Thiede, R., Bookhangen, B., Arrowsmith, J.R, Sobel, E., & Strecker, M.R. (2004). Climatic control on rapid exhumation along the southern Himalayan front. Earth Planet. Sci. Lett, 222, 791–806.

Todd, S.P. (1989). Stream-driven, high-density gravelly traction carpets: possible deposits in the Trabeg Conglomerate Formation, SW Ireland and some theoretical considerations of their origin. Sedimentology (IAS), 36, 513-735.

Tofelde, S., Schildgen, T.F., Savi, S., Pingel, H., Wickert, A.D., Bookhangen, B., Wittmann, H., Alonso, R.N., Cottle, J., & Strecker, M.R. (2017). 100kyr fluvial cut-and-fill terrace cycles since the Middle Pleistocene in the southern Central Andes, NW Argentina. Earth Planet. Sci. Lett, 473, 141–153.

Verdel, C., Wernicke, B.P., Hassanzadeh, J., & Guest, B. (2011). A Paleogene extensional arc flare-up in Iran. Tectonics, 30, TC3008.

Vincent, P. (2004). Present-day crustal deformation and plate kinematics in the Middle East constrained by GPS measurements in Iran and north ern Oman, Geophys. J. Int, 157, 381–398.

Vincent, S.J., Morton, A.C., Carter, A., Gibbs, S., & Barabadze, T.G. (2007). Oligocene uplift of the western Greater Caucasus: An effect of initial Arabia– Eurasia collision. Terra Nova, 19, 160–166.

Whippe, K.X., & Meade, B.J. (2004). Controls on the strength of coupling among climate, erosion, and deformation in two-sided, frictional orogenic wedges at steadystate. J. Geophys. Res, 109, F1.

Willett., S.D. (1999). Orogeny and orography: The effects of erosion on the structure of mountain belts. J. Geophys. Res 104, 28957–28981.

Wilmsen, M., Fursichfranz, F.T., Fursich, T., Seyed-Emami, K., Majidifard, M.R., & Taheri, J. (2009). The Cimmerian Orogeny in northern Iran: Tectono-stratigraphic evidence from the foreland. Terra nova, 21, 211-218.

Yassaghi, A., & Madanipour, S. (2008). Influence of a transverse basement fault on along strike variations in the geometry of an inverted normal fault: Case study of the Mosha Fault, Central Alborz Range, Iran. J. Struct. Geol 30, 1507–1519.

Zanchi, A., Zanchetta, S., Berra, F., Mattei, M., Garzanti, E., Molyneux, S., Nawab, A., & Sabouri, J. (2009). the Eo-Cimmerian (Late? Triassic) orogeny in North Iran. Geological Society, London, Special Publication, 312, 31-55.